

# Improved High-resolution Fast Imager

Carsten Denker<sup>ⓧ, a,\*</sup>, Meetu Verma<sup>ⓧ, a</sup>, Aneta Wiśniewska<sup>ⓧ, a</sup>,  
Robert Kamlah,<sup>a,b</sup> Ioannis Kontogiannis<sup>ⓧ, a</sup>, Ekaterina Dineva<sup>ⓧ, a</sup>,  
Jürgen Rendtel,<sup>a</sup> Svend-Marian Bauer,<sup>a</sup> Mario Dionies,<sup>a</sup> Hakan Önel<sup>ⓧ, a</sup>,  
Manfred Woche,<sup>a</sup> Christoph Kuckein<sup>ⓧ, c</sup>, Thomas Seelemann,<sup>d</sup>  
and Partha S. Pal<sup>ⓧ, a,e</sup>

<sup>a</sup>Leibniz Institute for Astrophysics Potsdam (AIP), Potsdam, Germany

<sup>b</sup>University of Potsdam, Institute of Physics and Astronomy, Potsdam, Germany

<sup>c</sup>Instituto de Astrofísica de Canarias (IAC), Tenerife, Spain

<sup>d</sup>LaVision GmbH, Göttingen, Germany

<sup>e</sup>Bhaskaracharya College of Applied Sciences (University of Delhi),  
Dwarka, New Delhi, India

**Abstract.** The improved High-resolution Fast Imager (HiFI+) is a multiwavelength imaging filtergraph, which was commissioned at the GREGOR solar telescope at Observatorio del Teide, Izaña, Tenerife, Spain, in March 2022 – followed by science verification in April 2022, after which it entered routine observations. Three camera control computers with two synchronized sCMOS and CMOS cameras each provide near diffraction-limited imaging at high cadence in six wavelength bands (Ca II H at 396.8 nm, G-band at 430.7 nm, blue continuum at 450.6 nm, narrow- and broad-band H $\alpha$  at 656.3 nm, and TiO bandhead at 705.8 nm). This unique combination of photospheric and chromospheric images provides “tomographic” access to the dynamic Sun and complements spectropolarimetric observations at the GREGOR telescope. High image acquisition rates of 50 and 100 Hz facilitate image restoration, where time series of restored images have a typical cadence of 6 and 12 s, which is sufficient to resolve the dynamics of the solar photosphere and chromosphere. In principle, all imaging channels can be restored individually using the speckle masking technique or multiframe blind deconvolution (MFBD). However, images recorded strictly simultaneously in the narrow-/broad-band H $\alpha$  and the G-band/blue continuum channels can be pairwise subjected to multiobject multiframe deconvolution (MOMFBD) expanding the science capabilities of HiFI+. For example, the narrow-band (FWHM = 60 nm) Halle H $\alpha$  Lyot filter isolates the H $\alpha$  line core, which facilitates matching chromospheric fibrils and filamentary structures to photospheric bright points. Likewise, dividing G-band by blue continuum images enhances small-scale brightenings, which are often related to small-scale magnetic fields so that their evolution can be tracked in time. A detailed description of the improved high-cadence, large-format imaging system is presented and its performance is assessed based on first-light observations. © The Authors. Published by SPIE under a Creative Commons Attribution 4.0 International License. Distribution or reproduction of this work in whole or in part requires full attribution of the original publication, including its DOI. [DOI: [10.1117/1.JATIS.9.1.015001](https://doi.org/10.1117/1.JATIS.9.1.015001)]

**Keywords:** Sun: photosphere; Sun: chromosphere; instrumentation: high angular resolution; instrumentation: detectors techniques: image processing; atmospheric effects.

Paper 22099G received Oct. 13, 2022; accepted for publication Jan. 12, 2023; published online Feb. 7, 2023.

## 1 Introduction

In the consumer market, CMOS detectors have already replaced CCD sensors in many applications. This transition from CCD to CMOS technologies is also happening in astronomical and solar instrumentation because the noise characteristics of the CMOS devices significantly improved in recent years.<sup>1–3</sup> Fast, large-format CMOS detectors reach and exceed full High Definition (HD) resolution (1920 × 1080 pixels) and can achieve image acquisition rates of

---

\*Address all correspondence to Carsten Denker, [cdenker@aip.de](mailto:cdenker@aip.de)

50–100 Hz. Such camera systems are ideally suited for current high-resolution solar telescopes, which rely on adaptive optics (AO)<sup>4</sup> and image restoration<sup>5</sup> to reach diffraction-limited performance across a field-of-view (FOV) of about 100" in diameter. Even though the AO correction decreases with distance from the lock point,<sup>6,7</sup> partial AO correction still aids image restoration across a large FOV. In addition, image restoration methods were developed and delivered near diffraction-limited data even before AO systems were available, and nowadays the methods include a proper treatment for the optical transfer function (OTF) with AO correction.

Spectral imaging of the solar chromosphere in the visible and near-infrared requires narrow-band filters with passbands  $\Delta\lambda < 0.1$  nm. Such narrow passbands facilitate isolating the line cores of strong chromospheric absorption lines such as Ca II H at 396.8 nm, H $\alpha$  at 656.3 nm, and He I at 1083.0 nm,<sup>8–10</sup> among others. In 1933, Lyot<sup>11</sup> introduced the first narrow-band filter for solar spectral imaging combining birefringent and polarizing elements. The working principle of the filter was independently discovered by Öhman.<sup>12</sup> Since then, Lyot-Öhman filters were commonly used at solar observatories around the world. The Universal Birefringent Filter (UBF) can be considered as an intermediate step between Lyot-Öhman filters and Fabry-Pérot interferometers.<sup>13</sup> However, only the latter can achieve a higher photon flux per diffraction-limited pixel. An example is the single-etalon visible imaging magnetograph (VIM)<sup>14</sup> at the 1.6-meter Goode solar telescope (GST), nowadays called visible imaging spectrometer (VIS), which is mainly used as an H $\alpha$  spectrometer with a passband of  $\Delta\lambda = 7$  pm. A high-transmission and narrow-band (about 0.3 nm passband) interference filter is used to eliminate side-lobes. Nowadays, advanced thin film deposition techniques for dielectric materials enable the production of interference filters with passbands of  $\Delta\lambda < 0.05$  nm, which can be directly used to observe the cores of strong chromospheric absorption lines.<sup>15</sup>

High-resolution imaging with Lyot-Öhman filters becomes challenging because of the low filter transmission, which significantly reduces the photon flux for diffraction-limited imaging. Thus, it becomes difficult to achieve short exposure times of just a few milliseconds, which are required to “freeze” the seeing—a common assumption for image restoration applications such as speckle masking imaging,<sup>16–18</sup> speckle deconvolution,<sup>19</sup> and blind deconvolution techniques.<sup>20,21</sup> Nonetheless, the rapid oscillations in the solar atmosphere (ROSA)<sup>22</sup> instrument at the 0.7-meter Dunn solar telescope (DST) successfully employs a UBF and an H $\alpha$  Lyot filter. Dual-channel imagers can mitigate the effects of low photon flux on image restoration. Using two strictly synchronized cameras facilitates to restore the broad- and narrow-band channels of an imaging system simultaneously, benefiting from the high signal-to-noise ratio in the broad-band channel. Thus, the atmospheric turbulence and the seeing conditions can be characterized with high confidence, enabling the restoration of the noisier filtergrams that were recorded, e.g., with Lyot-Öhman filters. The broad-band channel also serves as an anchor for the restoration of the narrow-band images when scanning spectral line profiles.

Instruments for high-spatial resolution imaging belong to the standard equipment of solar telescopes, e.g., the ROSA instrument at DST or the visible broadband imager (VBI)<sup>23</sup> at the 4-meter *Daniel K. Inouye Solar Telescope* (DKIST).<sup>24</sup> Larger telescope apertures impact the optical design of the imagers and pose challenges for image restoration.<sup>25</sup> While the light gathering power of a telescope increases proportional to the aperture diameter squared, observing at the diffraction limit opposes this effect. Thus, the number of photons per diffraction-limited pixel is independent of the aperture size. However, the angular size of a diffraction-limited pixel becomes smaller for larger telescope apertures. Image restoration assumes that the observed solar feature does not evolve. Thus, the atmospheric sound speed imposes a limit for the image acquisition time of just a few seconds, i.e., the time for a solar feature to traverse a pixel, which is already hard to meet for observations with the GREGOR telescope. For a telescope such as DKIST, the image acquisition time for image restoration may already become too short to gather sufficient images with independent realizations of the distorted wavefronts. In this article, initial results are presented from the improved High-resolution Fast Imager (HiFi+) at the 1.5-meter GREGOR solar telescope.<sup>26–28</sup> The imaging system was designed to monitor the solar photosphere and chromosphere with high spatial and temporal resolution in six wavelength bands. The instrument description includes the optical layout, the sCMOS and CMOS camera systems including control computers and software, and data processing and archiving. The new HiFi+ entered routine observations starting with the first observing semester of 2022.

## 2 Optical Design

### 2.1 GREGOR Solar Telescope

The 1.5-meter GREGOR solar telescope (Fig. 1) was inaugurated in 2012 and started routine science observations two years later in 2014. Detailed descriptions of the telescope and its initial suite of postfocus instruments<sup>29–31</sup> were published in Volume 333 of the *Astronomische Nachrichten/Astronomical Notes* and the first science results were presented in Volume 596 of *Astronomy & Astrophysics*. GREGOR's suite of high-resolution imagers, a two-dimensional spectrometer, and an infrared spectrograph was continuously improved. In 2018, remodeling of the optical laboratory was initiated to address some long-standing optical design issues and to prepare the GREGOR telescope for the next generation of instruments.<sup>32</sup> The light distribution system of GREGOR now includes three plate beamsplitters on a rotary stage, where one has a 1:1 splitting ratio and the other two are dichroic ones with cutoff wavelengths of 650 and 900 nm, respectively. The reflected light is directed to HiFI+. In the following, the optical layout of HiFI+ (Fig. 2) is described in detail.

### 2.2 Dual-channel Design of the Imager

To sample the optical image at the diffraction limit, the pixel scale (in arcseconds per pixel) must be adapted for the observed wavelengths. The range from 400 to 700 nm implies a change in the pixel scale of almost a factor of two. Since the size of a pixel is fixed and given by the selected camera, the plate scale (in arcseconds per millimeter) at the detector must be adapted accordingly. Alternatively, oversampling and binning in the red will enable the use of a fixed plate scale optimized for the blue at the cost of wasted sensor pixels in the red. The first option was selected for HiFI+, which divides the incoming beam into a red imaging channel and into a blue imaging channel with separately adapted plate scales.



**Fig. 1** The 1.5-meter GREGOR solar telescope at Observatorio del Teide, Izañā, Tenerife, Spain. The foldable tent dome is retracted, and the telescope is pointing toward the Sun.



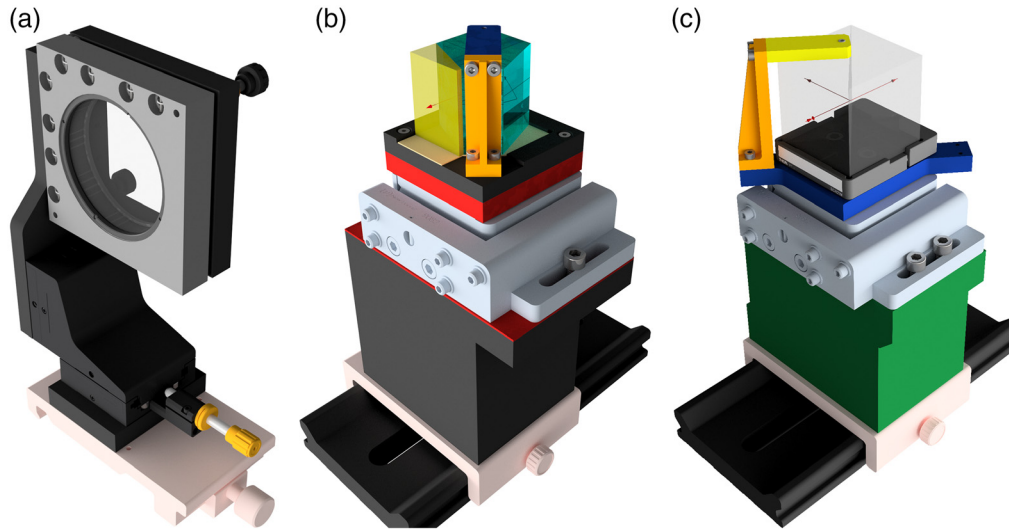


**Fig. 3** (a) The mounts for achromatics lenses, (b) the pentaprism, and (c) the beamsplitters are based on off-the-shelf-components, which provide all needed adjustments, i.e., translation, tip-tilt, and rotation for the pentaprism and beamsplitters. Only the lens holders and adapters to the carriers of the L95 rail system were manufactured in house.

splitting ratio and a 50 mm edge length. It sends 20% of the light to the TiO channel, where the respective interference filter is placed directly in front of the CMOS camera. The beamsplitter mounts (right panel of Fig. 3) use the same compact five-axis alignment stages as the pentaprism mount. The characteristics of the interference filters are listed in Table 1. A broad-band  $H\alpha$  interference filter is placed between the first and second cube beamsplitters. Both beamsplitters have identical properties so that 20% of the light is sent to the broad-band  $H\alpha$  channel, whereas the remainder of the light passes through the narrow-band  $H\alpha$  Lyot filter. The two cube beamsplitters with the 4:1 splitting ratio are custom-made and were manufactured by EKSMA Optics in Vilnius, Lithuania. The  $H\alpha$  interference filter acts in this case as an order-sorting filter for the Lyot filter. The narrow-band ( $\Delta\lambda = 60$  pm)  $H\alpha$  filtergrams are obtained with a Lyot filter manufactured in 1945 and modified later by Bernhard Halle Nachf., Berlin-Steglitz.<sup>33</sup> The Halle filter No. 22 was originally located at the solar observatory Einstein Tower<sup>34</sup> but was transferred to Observatorio del Teide for high-resolution imaging. The filter is temperature controlled, and the wavelength can be tuned by changing the temperature. Tuning the filter in a narrow wavelength

**Table 1** Characteristics of interference filters, which are used in HiFI+. The pixel scale indicates that, with exception of  $H\alpha$  images, all images are critically sampled with respect to the diffraction limit  $\lambda/D$ . Note that the Imager M-lite 2M cameras use only an ROI of  $1536 \times 1216$  pixels in the red imaging channel to completely fit within the  $100''$ -diameter FOV of the  $F_3$  field stop.

	Ca II H	G-band	Blue continuum	$H\alpha$	TiO
$\lambda$	396.8 nm	430.7 nm	450.6 nm	656.3 nm	705.8 nm
$\Delta\lambda$	1.080 nm	1.120 nm	1.150 nm	0.750 nm	0.946 nm
$\lambda/D$	0.057''	0.062''	0.065''	0.094''	0.101''
Plate scale		4.25'' mm <sup>-1</sup>		8.50'' mm <sup>-1</sup>	
Pixel scale	0.025'' pixel <sup>-1</sup>		0.028'' pixel <sup>-1</sup>	0.050'' pixel <sup>-1</sup>	
FOV	48.2'' $\times$ 30.8''		70.7'' $\times$ 59.6''	76.5'' $\times$ 60.5''	
Max. transmission	63.8%	54.4%	64.5%	70.0%	68.8%
Serial No.	159203	158885	158886	LQ166-01	CC147-10

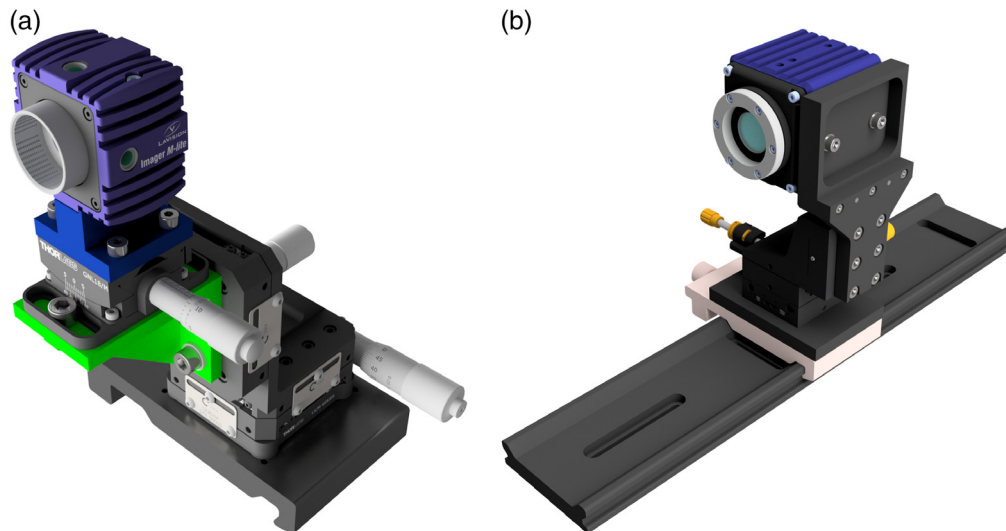


**Fig. 4** (a) The Imager M-Lite 2M and (b) Imager sCMOS cameras are mounted on precision  $x, y, z$ -translation stages. The mount of the Imager M-Lite 2M camera also includes a goniometer, which provides a  $\pm 5$  deg rotation of the detector around the optical axis. All camera mounts are attached to L95 rails on optical tables to ease optical alignment.

range can also be accomplished by rotating a polarizer on the Sun-facing side of the filter. By turning a second polarizer by 90 deg at the exit of the filter, the bandpass can be changed from the default 60 to 120 pm.

Since identical CMOS cameras are used for  $H\alpha$  and TiO observation, all three CMOS cameras of the red imaging channel have the same pixel scale of  $0.050'' \text{ pixel}^{-1}$ . A region-of-interest (ROI) of  $1536 \times 1216$  pixels is selected to adapt to the beam size, which results in a FOV of  $76.5'' \times 60.5''$ . The TiO images in the red imaging channel are critically sampled according to the Nyquist-Shannon sampling theorem, when the criterion  $\lambda/D$  for the angular resolution is used, where  $\lambda$  is the observed wavelength and  $D = 1.44$  m is the diameter of the aperture stop in front of GREGOR's primary mirror. However, the images in the  $H\alpha$  narrow- and broad-band channels are slightly undersampled by 6%. All four CMOS cameras are mounted on precision linear  $x, y, z$ -stages with Vernier micrometers for centering and focusing. An additional goniometer provides a  $\pm 5$  deg rotation of the detector around the optical axis (left panel of Fig. 4), which is important for the precise alignment of the  $H\alpha$  narrow- and broad-band cameras, when using MOMFBD for image restoration.

The given pixel size of the cameras and the smaller pixel scale required for diffraction-limited imaging leads to a more compact setup of the blue imaging channel. The 1:2 transfer optics with two achromatic lenses ( $f = 250$  and  $500$  mm) reduces the plate scale by a factor of two, i.e., the plate scale is  $4.25'' \text{ mm}^{-1}$ . The compact setup also requires that the pupil  $P_4$  is not at infinity when viewed from the second lens of the transfer optics. In all other cases, either the pupil or focal plane is at infinity when viewed from the respective lenses. Since the Ca II H line-core intensity and also the intensity in the inner line wings is very low, a relatively broad interference filter with a passband of  $\Delta\lambda \approx 1$  nm ensures a photon flux sufficient for image restoration. Consequently, the first beamsplitter in the blue imaging channel has a 4:1 splitting ratio so that the Ca II H channel receives 80% of the incoming light. The full detector size of  $1936 \times 1216$  pixels can be used because of the reduced pixel scale of  $0.025'' \text{ pixel}^{-1}$ . However, the FOV is still the smallest of all six imaging channels. The light reflected in the beamsplitter feeds the G-band and blue continuum channels, which receive light via another beamsplitter with a 1:1 splitting ratio. The sCMOS camera has a larger detector with  $2560 \times 2160$  pixels and a slightly different pixel scale of  $0.028'' \text{ pixel}^{-1}$  because of the slightly larger pixel size compared to the CMOS cameras. The camera mounts only have linear  $x, y, z$ -translation stage for alignment and focusing (right panel of Fig. 4), i.e., the rotational alignment of the G-band and blue continuum channels has to become part of the image processing. The FOV in the G-band and blue continuum channels is the same as is the case for all cameras in the red imaging channel.

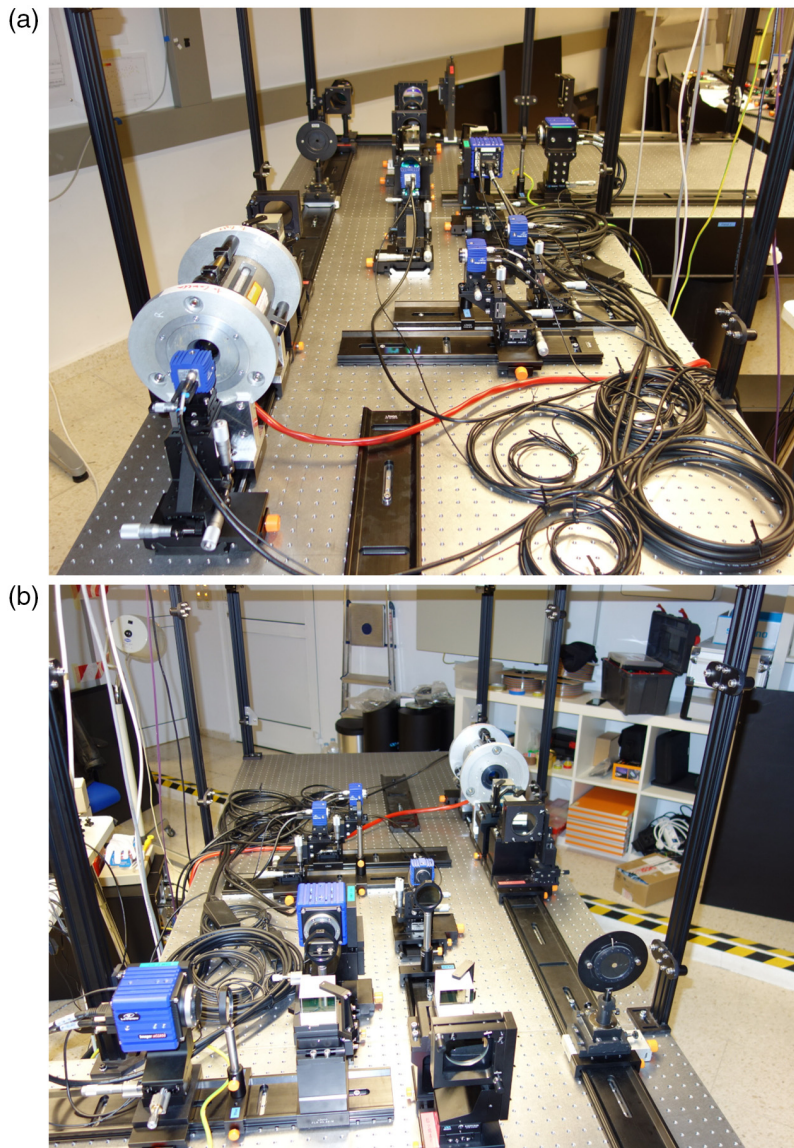


**Fig. 5** HiFI+ during assembly in November 2021. The blue imaging channel (b) shows the two Imager sCMOS cameras in the foreground and one of the Imager M-lite 2M cameras in the back. The  $H\alpha$  Lyot filter (gray cylinder with round aluminum mounting plates) is visible at the end of the optical table. The red imaging channel (a) includes the  $H\alpha$  Lyot filter and three Imager M-lite 2M cameras. The protective cover box was not yet installed but the vertical struts for mounting the side panels of the box are already present.

The completed optical setup of HiFI+ is depicted in Fig. 5, which provides front and rear perspectives, when HiFI+ is viewed along the long axis of the optical tables. The bottom panel shows the light distribution in the blue imaging channel, where the larger sCMOS cameras of the G-band and blue continuum channels are prominently visible in the lower-left corner. The CMOS camera of the Ca II H channel is located in the center of the picture. The top panel zooms in on the  $H\alpha$  Lyot filter and the three CMOS cameras of the red imaging channel. In addition to the pupil stops, black metal screens and baffles (not shown) are used to minimize stray light. The struts of the protective cover box are already mounted on the sides of the optical tables. The height of the box is 80 cm, which facilitates easy access to the opto-mechanical elements when the side panels of the box are removed. The box mainly protects the instruments from dust but also stabilized to some extent the temperature inside the box. The  $H\alpha$  Lyot and the cameras are the only heat sources inside the cover box. The CMOS cameras and the Lyot filter are always

turned on, resulting in a temperature of about 3 °C above ambient, whereas the sCMOS cameras are only turned on during observations, to maximize the lifetimes of their cooling fans. This leads to an additional temperature increase of about 2 °C. Once all cameras are running and sunlight enters the instrument, the temperature reaches an equilibrium after about 30 min, with temperature changes during the observations well below  $\pm 0.25$  °C. These temperature fluctuations do not affect the imaging performance of HiFI+.

### 2.3 Optical Alignment and Imaging Performance

A proper optical alignment of lenses, the pentaprism, and beamsplitters is essential for the optical quality of the images at the final focal planes. Thus, an optical ruler is used in the first step, where a HeNe laser is mounted at one end of an optical rail. The correct height and centering of the laser beam above a long optical rail is verified with a sliding target, which is subsequently mounted at the other end of the rail. The achromatic lens to be aligned is inserted in the laser beam using the linear  $x$ ,  $y$ -translation stages to keep the transmitted laser beam centered on the target. The adjustments of the kinematic mount are used to center the retro-reflection from the first surface of the lens. The same idea applies to aligning the pentaprism and beamsplitters. However, a second optical rail with its own target has to be introduced, which is exactly perpendicular to the first optical rail. After preliminary alignment, the optics are inserted one by one following the light path of HiFI+. The red imaging channel is aligned first, then the light is blocked just behind the pentaprism, before the blue channel is aligned. The position of the achromatic lenses is verified using auto-collimation. Only small adjustments are needed in this setup procedure. The final locations of the optical elements agree with those of a Zemax design of HiFI+. The spot diagrams in Fig. 6 demonstrate that a nearly diffraction-limited performance can be achieved in all imaging channels using off-the-shelf achromats for the transfer optics. The shorter wavelengths and the faster transfer optics leads to higher aberrations in the blue imaging channel, where spherical aberration is most distinctive on-axis, which turns into coma off-axis, especially in the corners of the FOV. The strongest aberrations appear in the blue continuum and G-band channels, where the latter is not shown because the spot pattern is almost the same.

The remainder of this section is intended to provide a critical appreciation of the tools and devices, which are available for validating proper alignment of the instrument and for verifying its imaging performance. The rotary stage in the focal plane  $F_3$  contains field stops of different diameters and a closed position to block the light beam so that dark frames can be taken. More importantly, it includes inserts for aligning the optics. A small pinhole with a diameter of 0.36 mm or about 1.3" defines the center of the FOV and the height above the optical tables, which is 205 mm. The small pinhole is used for calibrating the wavefront sensor and the AO system. It defines one point of the optical axis, and all opto-mechanical components have to be mounted such that the light path has a constant height above the optical tables and is centered along the optical rails. Thus, the small pinhole is the reference for centering the FOV on all detectors. In addition, a larger pinhole with a diameter of 2.1 mm or about 7.4" is available, which is currently not used. However, radial intensity profiles across the large pinhole encode the modulation transfer function (MTF), a common image quality metric, which can be retrieved similarly to the slanted-edge method.<sup>35</sup> Programs to determine the MTF in such a way are currently in development. Two more inserts, i.e., a pinhole grid and a modified USAF-1951 resolution target, facilitate further means for alignment and verifying imaging performance.

The MOMFBD algorithm assumes that narrow- and broad-band channels are aligned with good precision. To minimize interpolation errors, it is advantageous to align the cameras manually as good as possible. A pinhole grid target was designed for this task (see upper-right panel in Fig. 7). Pinholes are arranged in a square grid with an equidistant spacing of 1.4 mm. The pinhole grid is manufactured from spring steel with a diameter of 38 mm and a thickness of 0.1 mm. The positioning accuracy is  $\pm 0.03$  mm. The laser-cut pinholes have a diameter of 0.1 mm or about 0.35", with the exception of four pinholes arranged in an L-shape, where the diameter is 0.15 mm or about 0.53". The pinhole in the corner of the L marks the center of the FOV, and the L-shaped pinhole pattern breaks the symmetry of the target, which is important

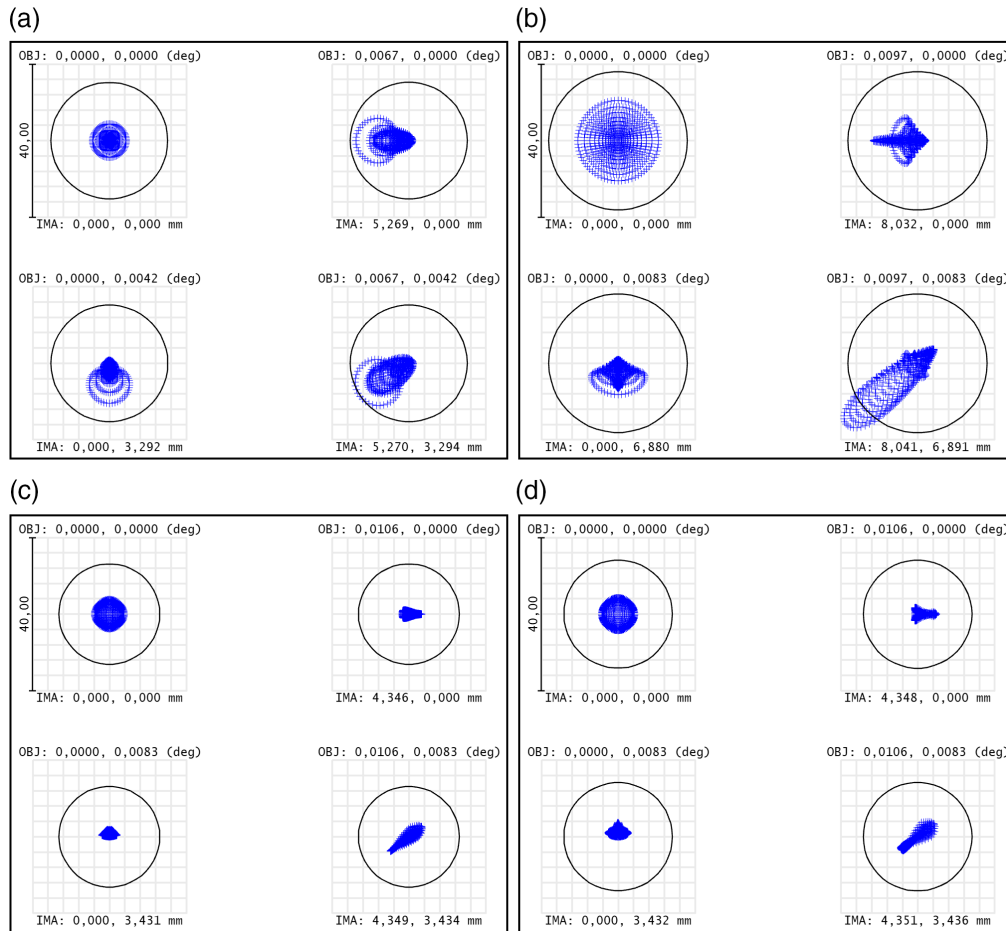


**Fig. 6** (a)–(d) Spot diagrams for the Ca II H at 396.8 nm, blue continuum at 450.6 nm, H $\alpha$  at 656.3 nm, and TiO bandhead at 705.8 nm imaging channels. Inside the panels, the on-axis performance is shown along with diagrams for the left side, top side, and top-right corner of the detectors.

when aligning mirrored or rotated images. Unfortunately, the pinhole grid target is not properly aligned with the detector orientation, i.e., a rotation offset of about 121 deg exists between pinhole target and detector.

Optical aberrations such as pincushion and barrel distortions can be determined from the pinhole grid. Each pinhole is fitted with a two-dimensional Gaussian using the MPFIT software package,<sup>36</sup> which provides the background level, the peak intensity, the coordinates of the pinhole, the FWHM along the short and long axes, and the rotation angle of the long axis. In total, 186 pinholes were fitted excluding some pinholes at the periphery. The estimated precision of the algorithm for the coordinates is about one fifth of a pixel. The pinholes are close to circular across the FOV, and the rotation angle does not show any preferred direction or pattern. The grid spacing is  $(100.29 \pm 0.20)$  pixels and  $(100.32 \pm 0.44)$  pixels for the pinhole target in the H $\alpha$  narrow- and broad-band channels, respectively. This corresponds to  $(1.4106 \pm 0.0042)$  mm and  $(1.4109 \pm 0.0062)$  mm, considering the demagnification by a factor of 2.4 in the image plane and that the pixel size of  $5.86 \mu\text{m} \times 5.86 \mu\text{m}$  is taken at face value. Taking into account various error sources and manufacturer specified values, the measured grid spacing agrees very well with the designed grid spacing of the pinhole grid target. However, the black vectors in the left panel of Fig. 7 clearly indicate that optical aberrations have distorted the equidistant pinhole grid. The average deviation of the observed pinhole location from an equidistant grid is  $(1.26 \pm 0.56)$  pixels, where the standard deviation indicates the variation of the measured distances rather than an error estimate. Such minor distortions are, however, negligible considering the science requirements of HiFI+. The difference map that is used as the

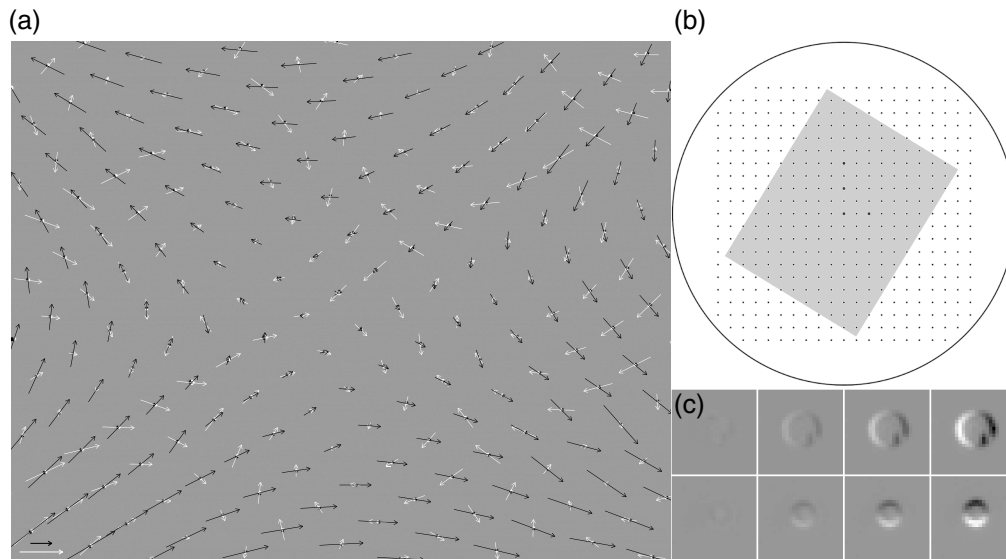


**Fig. 7** (a) Difference map of aligned pinhole grids in the narrow- and broad-band  $H\alpha$  channels. The white vectors show the misalignment between the two grids, whereas the black vectors show the deviations of the narrow-band  $H\alpha$  grid from a perfect grid with equidistant spacing, i.e., they represent the optical aberrations introduced between the focal plane  $F_3$  and the detector. The two horizontal vectors in the lower-left corner have a length of one pixel. The layout of the pinhole grid (b) is displayed with the superposed FOV of the red imaging channel (light gray rectangle). Zoomed-in difference maps (c) of a large pinhole (top row) and a small pinhole (bottom row). The pinholes are displaced horizontally (top row) and vertically (bottom row) by 0.0, 0.2, 0.5, and 1.0 pixel. The difference maps are scaled with respect to the rightmost maps.

background in Fig. 7 demonstrates the good interalignment of the two pinhole grid targets. The average displacement of the pinholes, as indicated by the white vectors, is only  $(0.43 \pm 0.19)$  pixels. Closer inspection reveals a pattern with a characteristic size of about 500 pixels, where the displacements reach a local minimum. The only optical elements that can contribute to this pattern are the final beamsplitter and the Lyot filter. Minor optical aberrations introduced by the  $H\alpha$  interference filter may be altered by the different optical path length differences, when the light passes through the beamsplitter and the Lyot filter. The eight small panels in the lower-left part of Fig. 7 visualize the impact of horizontally and vertically misaligned pinholes. A live image of the difference map is thus a very helpful tool in manually aligning the detectors on the pinhole grid target. The black-and-white pattern of each pinhole gives an immediate feedback on the shift, rotation, and magnification of the two detectors. Since the plate scale and pixel scale of all three cameras in the red imaging channel are the same, they can be easily aligned, i.e., only the cable connections of the TiO and  $H\alpha$  narrow-band cameras have to be temporarily exchanged for this task.

The spatial resolution and low-order optical aberrations can be measured using a USAF-1951 resolution target. Distributing several targets across the FOV (Fig. 8) facilitates additionally measuring the field dependence of the spatial resolution and optical aberrations. The smudged marks of a felt-tip pen, which surround the central target, break the symmetry of the pattern, which is helpful when aligning image channels with mirrored or rotated targets. The elements of the 5<sup>th</sup> group in the target represent 32.0, 35.9, 40.3, 45.3, 50.8, and 57.0 line pairs per millimeter, which corresponds to 9.0, 10.1, 11.4, 12.8, 14.4, and 16.1 line pairs per arcsecond using the plate scale of the focal plane  $F_3$ . The corresponding spatial resolution is given by 0.111, 0.099, 0.088, 0.078, 0.070, and 0.062 arcsec, respectively. The fifth element of the fifth group is only just resolvable in Fig. 8 for the blue imaging channel, where the diffraction-limited spatial resolution is  $\lambda/D = 0.065''$ . The minute separation of the three-bar pattern is much easier to see in live images, where the contrast and zoom can be manually adjusted. Thus, the imaging performance is very close to the theoretical prediction. A comparison of the central target with the peripheral targets yields a similar resolution across the FOV, and no field-dependent aberrations

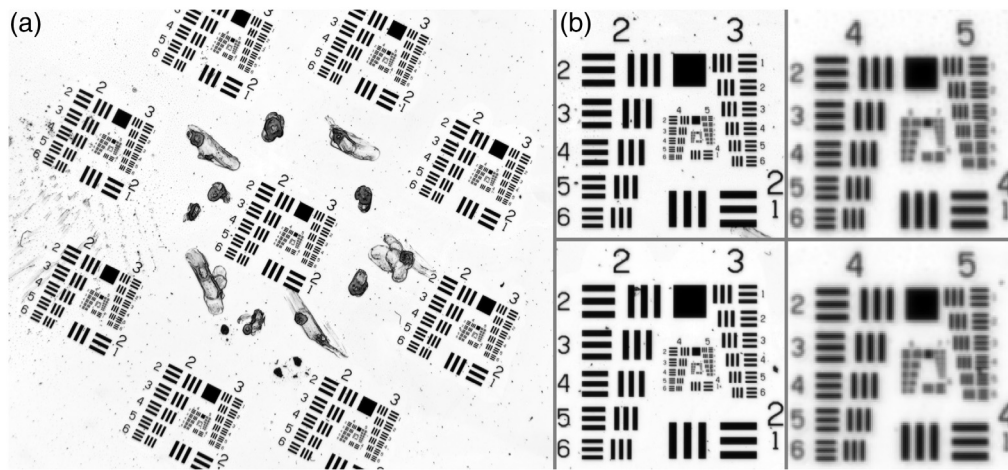


**Fig. 8** The spatial resolution in the imaging channels is validated using a modified USAF-1951 resolution target (a), i.e., in this example, in the blue continuum channel. A central target is surrounded by eight other targets to determine the image resolution across the FOV. Derotated and zoomed-in versions of the targets (b) show the central target (top row) and the upper-rightmost target (bottom row), zooming in on the full targets (left column) and their central regions (right column).

are evident in visual inspection. The blue imaging channel was chosen in this example because of its higher demands on the transfer optics, where the faster  $f$ -ratio of the transfer optics leads to stronger aberrations (see the upper-right panel in Fig. 6).

## 2.4 Interference Filters

The characteristics of the interference filters are laid out in Table 1. However, for the scientific interpretation of the high-resolution image time-series, the spectral range that is transmitted by the filter has to be known. Figure 9 summarizes the properties of the filter, as provided by the filter curves of the manufacturers, along with the covered spectral regions taken from spectral atlases. The top panel clearly illustrates the low photon flux for observations of the inner line wings and line core of the strong chromospheric absorption line Ca II H. The middle panels demonstrate quite strikingly the differences between the Fraunhofer G-band, which is dominated by tightly packed lines of the CH molecule, and the blue continuum region, which is relatively sparsely populated by spectral lines. The term “continuum” should be taken with caution because in the blue part of the solar spectrum no region exists, which is void of spectral lines. The selected spectral region is, however, the best choice with the lowest contribution from spectral lines. The H $\alpha$  narrow- and broad-band channels play a special role in HiFI+ because MOMFBD is the standard method for image restoration. Unfortunately, the H $\alpha$  interference filter is not exactly centered at the H $\alpha$  line core, so the filter has to be tilted, which results in a broader transmission profile with a lower peak transmission. If the 650 nm beamsplitter of the GREGOR light distribution system is used, then imaging in the H $\alpha$  channel is photon starved so that observations are not possible. Finally, the spectral features covered by the TiO filter differ drastically for quiet-Sun and sunspot regions because of the much cooler temperatures in sunspot umbrae. The light level in the TiO channel is also dramatically reduced by a factor of 12 when the aforementioned 650 nm beamsplitter is used. However, the light level is still sufficient for short exposure times (<10 ms), which are required for image restoration. In summary, (1) the blue continuum channel offers the best approximation of the continuum radiation with the highest spatial resolution, (2) the images taken in the Ca II H, G-band, and TiO channels exhibit small-scale brightenings, which are often but not always related to small-scale magnetic fields,<sup>40–42</sup> and (3) the H $\alpha$  narrow- and broad-band channels isolate chromospheric brightenings and the Lyot filter provides access to a wide variety of dynamic chromospheric absorption structures.

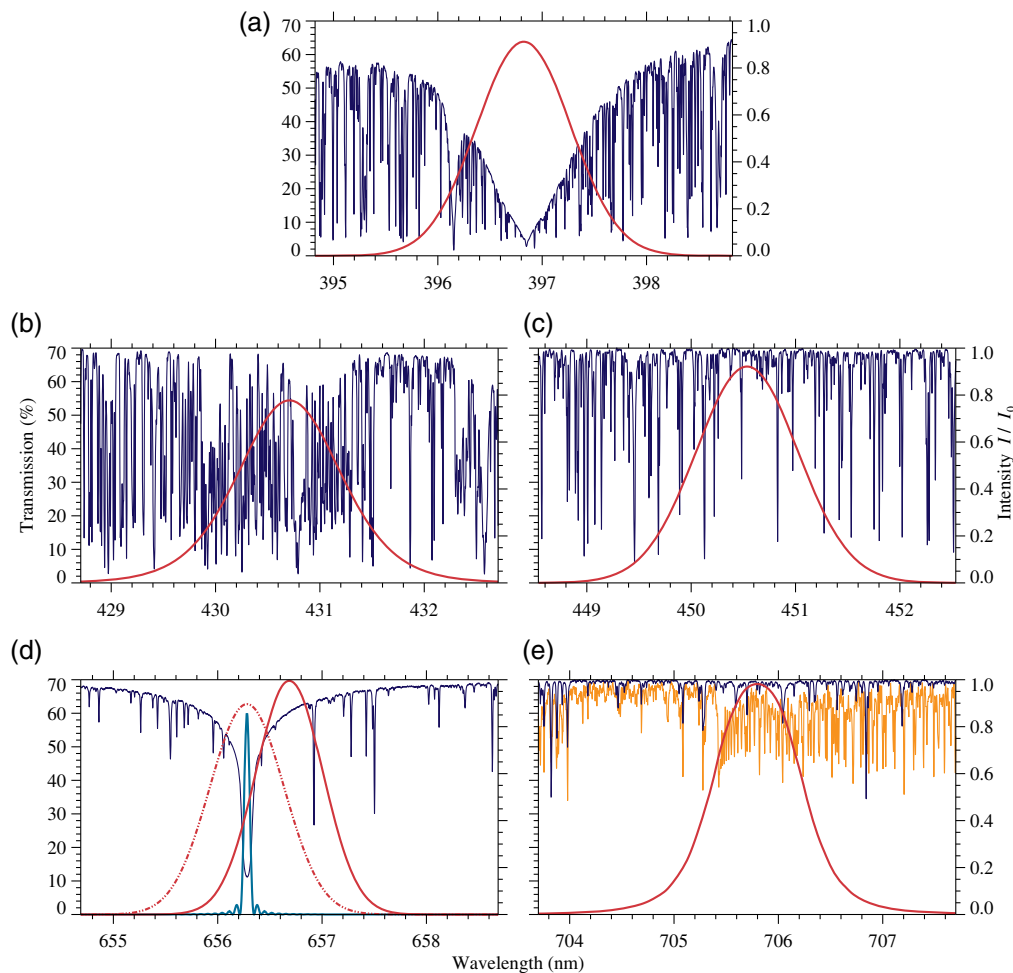


**Fig. 9** (a)–(e) Transmission curves (red) of the interference filter used in HiFI+: Ca II H at 396.8 nm, G-band at 430.7 nm, blue continuum at 450.6 nm, H $\alpha$  at 656.3 nm, and TiO bandhead at 705.8 nm. The Kitt Peak FTS disk-center spectral atlas<sup>37,38</sup> (blue) and the Kitt Peak near infrared spectral atlas of a sunspot<sup>39</sup> (orange) are provided for reference. The latter provides the exact location of the TiO bandhead. The transmission curve of the H $\alpha$  Lyot filter (light blue) was multiplied by 10 in intensity for better display. Since the central wavelength of the H $\alpha$  interference filter does not match the H $\alpha$  line core, the filter has to be tilted so that the maximum of the transmission curve (red dash-dotted) becomes lower and the bandpass becomes broader.

### 3 Camera Systems

The idea to improve the imaging capabilities of the GREGOR solar telescope was closely tied to the remodeling of its optical laboratory. With a new Fabry-Pérot interferometer on the horizon, covering an almost identical wavelength range as the GREGOR Fabry-Pérot Interferometer (GFPI)<sup>30,43</sup>, the decision to discontinue the GFPI became imminent. Currently, the option is explored to adapt the Fabry-Pérot etalons<sup>44</sup> for imaging spectropolarimetry in the blue part of the solar spectrum, building on an existing design for the blue imaging solar spectrometer (BLISS).<sup>45</sup> As a result, the two Imager M-lite 2M CMOS cameras of the GFPI and the two Imager sCMOS cameras of the original HiFI<sup>46,47</sup> became available. The purchase of two additional Imager M-lite 2M CMOS cameras with the same specifications as the CMOS cameras of the GFPI facilitates an instrument design with six channels that covers distinct photospheric and chromospheric morphological features in fine detail.

The characteristic parameters of the Imager M-lite 2M CMOS and Imager sCMOS cameras are based on data sheets<sup>48,49</sup> and camera manuals<sup>50,51</sup> provided by the manufacturer of the camera systems, i.e., LaVision GmbH in Göttingen, Germany. Both cameras are operated in global shutter mode. A comparison of both camera systems is provided in Table 2, which also demonstrates

**Table 2** Characteristics of the HiFi+ cameras, which feature fast image acquisition rates suitable for image restoration and detectors adapted to the 100"-diameter FOV and the diffraction limit of the GREGOR telescope.

	Imager M-lite 2M	Imager sCMOS
Number of cameras	4	2
Control software	LaVision DaVis 10.2	
Detector	Sony Pregius IMX 174	Fairchild Imaging CIS2051
Detector type	CMOS	sCMOS
Interface board	Fresco Logic FL1100	Silicon Software microEnable IV VD4-CL
Interface type	4 × USB3.0	2× Dual-port CameraLink
Max. data transfer rate	4 × 380 MB s <sup>-1</sup>	2 × 850 MB s <sup>-1</sup>
Number of pixels	1936 × 1216 pixels	2560 × 2160 pixels
Pixel size	5.86 μm × 5.86 μm	6.5 μm × 6.5 μm
Detector size	11.3 mm × 7.1 mm	16.6 mm × 14.0 mm
Max. frame rate (full ROI)	164/110 Hz	49 Hz
Max. quantum efficiency	77% @ 500 nm	57% @ 500 nm
Full well capacity	32,000 e <sup>-</sup>	30,000 e <sup>-</sup>
Read noise	7.0 e <sup>-</sup>	2.2 e <sup>-</sup>
Dynamic range	73.2 dB (1:4570)	82.7 dB (1:13,640)
Digital output	8/12 bit	16 bit
Exposure time	34 μs... 10 s	15 μs... 100 ms

that the Imager M-lite 2M CMOS and Imager sCMOS cameras are well adapted to the plate scale and maximum FOV of the red and blue imaging channels, respectively. Only in the Ca II H channel, a camera with a larger number of pixels covering a larger FOV would be desirable. However, the lower dead time, i.e., the time when no photons are collected during an exposure cycle, and the higher image acquisition rate of the Imager M-lite 2M CMOS camera is advantageous because of the more challenging seeing conditions in the very blue part of the solar spectrum. The coherence length, i.e., the Fried-parameter, scales with  $r_0 \sim \lambda^{6/5}$ . The same scaling applies to the coherence angle  $\theta_0$ , i.e., the angular extent of the isoplanatic patch, and the coherence time  $t_0$ , i.e., the time over which the wavefront tilt in an isoplanatic patch can be assumed to be constant. Thus, an improved statistics of the wavefront variations during a given time interval can be expected of the Imager M-lite 2M CMOS cameras as compared to the Imager sCMOS cameras. A programmable timing unit (PTU)<sup>52</sup> is installed on all computers, which synchronizes the image capture of the cameras with a precision of 10 ns. Image restoration with MOMFBD requires that the exposure times in both channels are the same.

The quantum efficiency of the Sony Pregius IMX 174 detector is depicted in Fig. 10. The quantum efficiency is about 58% in the Ca II H channel, about 59% in the H $\alpha$  narrow- and broadband channels, and about 38% in the TiO channels. The full well capacity of a pixel is 32000 e<sup>-</sup>, which is well adapted for the low light levels encountered with narrow-band filters such as Lyot filters, or even with interference filters with a moderately narrow passband of  $\Delta\lambda \approx 1$  nm, when observing strong chromospheric absorption lines. The Imager M-lite 2M CMOS cameras have a custom camera body, which acts as a heat sink. Since the cameras are continuously running, the heat dissipation via the camera body's surface is sufficient to keep the detector at a constant temperature. The low read noise of about 6.8 e<sup>-</sup> facilitates image restoration using

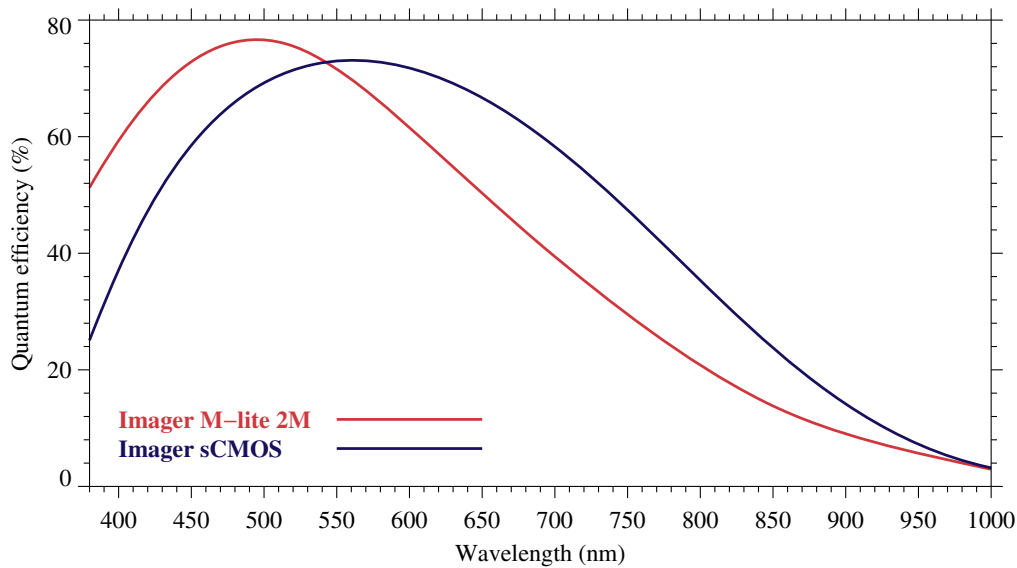


**Fig. 10** Quantum efficiency curves of the Imager M-lite 2M<sup>50</sup> and Imager sCMOS<sup>48</sup> cameras. The data are taken from product manuals and data sheets and are subsequently smoothed to show the general trend more clearly. Deviations by a few percent points should be expected locally.

either speckle or blind deconvolution techniques, even when the photon flux is low, e.g., in the umbra of sunspots or when observing in the cores of strong absorption lines. In both cases, the intensity drops by a factor of five or more compared to the quiet Sun and the continuum intensity, respectively.

The quantum efficiency of the Fairchild Imaging CIS2051 detector is depicted in Fig. 10. The quantum efficiency is about 52% in the G-band channel and about 59% in the blue continuum channel. Based just on the quantum efficiency, the CIS2051 detector would be the better choice for imaging wavelengths above 550 nm. However, the larger number of pixels makes the Imager sCMOS cameras the better choice for the blue part of the spectrum because of the smaller size of a diffraction-limited pixel. The detector of the sCMOS cameras is kept at a constant temperature using Peltier cooling and forced air for heat removal. The cameras are turned on just for the observations to prevent wear of the cooling fan, and it takes about 20 min to reach a constant temperature of the detector of about +5 °C. Two amplifiers for the low and high bits maximize the dynamic range and minimize the noise in the analog-digital conversions of the sCMOS cameras (cf. Table 2 for a comparison with the Imager M-lite 2M CMOS camera).

Assuming that the observed object does not change in a set of images, image restoration uses information about the noise statistics and about the seeing, which is “frozen” in short-exposure images, to retrieve an approximation of the true object. The dark current of about  $6 \text{ e}^- \text{ s}^{-1}$  and  $2 \text{ e}^- \text{ s}^{-1}$  for the Sony Pregius IMX 174 and Fairchild Imaging CIS2051 detectors, respectively, is inconsequential for typical exposure times below 10 ms, which is already an upper limit for image restoration considering the evolution timescale of Earth’s turbulent atmosphere. The chip architectures of CMOS and CCD devices differ, whereby CMOS detectors may exhibit a strong pixel-to-pixel dependence on the noise characteristics. However, based on existing experience, the noise filters and noise estimates implemented in speckle and blind deconvolution image restoration algorithms are not affected by this issue. In general, the photon noise will dominate the captured data. However, in dark structures such as sunspot umbrae and strong chromospheric absorption features, and in particular in the cores of spectral lines, the photon flux will be significantly reduced. Thus, the digitized read noise signal in the analog-digital conversions becomes increasingly important, which is, however, very low for this generation of CMOS and sCMOS cameras (Table 2). The dynamic range of the CMOS and sCMOS cameras is about 73 and 83 dB or about 1:4600 and 1:13,600, respectively, which is appropriate for image restoration, especially, considering that a large number of images (typically about 100 frames) is used as input for the image restoration procedures.

**Table 3** Specifications of the three HiFI+ camera control computers. Pixel packing and ROI read-out for the Imager M-lite 2M cameras are already considered in the actual data transfer rates to RAID 0 storage. The number of image pairs that can be stored already includes additional space for calibration data, i.e., the observing time refers to the duration of uninterrupted science observations excluding time for taking calibration data.

	HiFI+ No. 1	HiFI+ No. 2	HiFI+ No. 3
Channel	G-band/blue cont.	H $\alpha$	Ca II H/TiO
Camera	Imager sCMOS	Imager M-lite 2M	Imager M-lite 2M
Operating system	Microsoft Windows 10 Pro		
CPU	Intel E5-1650 v3	Intel Xeon W-2133	Intel Xeon E5-1650 v4
CPU launch date	Third quarter 2014	Third quarter 2017	Second quarter 2016
Clock speed	3.50 GHz/six cores	3.60 GHz/six cores	3.60 GHz/six cores
CPU benchmark	10,379/2116	12,270/2284	11,341/2377
Data transfer rate	1.1 GB s <sup>-1</sup>	560 MB s <sup>-1</sup>	630 MB s <sup>-1</sup>
RAID 0 storage (TB)	19.20	7.68	19.20
RAM	68.7 GB	34.4 GB	34.4 GB
Image pairs	860,000	1,350,000	3,000,000
Observing time (min)	340	275	600

The operating system of the camera control computers is Window 10 Pro, and the computer specifications are very similar. Any differences are mainly related to the date of purchase (Table 3). Today's computer technology makes it possible to record high-cadence, large-format images in real-time from computer memory to hard disk drives (HDDs) for HiFI+ No. 1 and 3 and solid-state drives (SSDs) for HiFI+ No. 2. However, vendor specifications are often not accurate and system integration of mainboard, CPU, RAID controller, disk drives, etc. may result in unexpected conflicts, thus limiting the system performance.

The CPU, mainboard, and other hardware components of the camera control computers were selected in such a way that on one hand sufficient PCIe lanes are available for graphics card, 10 Gigabit Ethernet card, RAID controller, PTU, and camera interface boards and on the other hand to have the highest possible computing power for real-time processing and evaluation of the data. The latter features are needed for camera alignment, calibration, and setting up optimized observing sequences. An external PTU with a USB 2.0 compliant interface had to be used because two dual-port CameraLink interface boards are used with the Imager sCMOS cameras. Another selection criterion is the performance during recording. Here CPU, mainboard, RAM, and disk drives/RAID system must be coordinated to ensure the maximum camera rate even with multicamera systems. The PassMark CPU benchmarks listed in Table 3 for multi- and single-core applications give an indication of the computing power, even though performance benchmarks are highly application specific. The DaVis camera control and imaging software<sup>53</sup> uses multithreading for streaming the image sets to RAID 0 storage. The best daytime seeing conditions at Observatorio del Teide are encountered about one hour after sunrise and last for about 1 to 2 h. On exceptional days, periods of very good to excellent seeing extend to about four hours. Furthermore, sometimes good seeing conditions occur a few hours before sunset. The RAID 0 storage of all HiFI+ camera control computers is well adapted to exploit the periods of good to excellent seeing conditions.

Observations at the GREGOR solar telescope can be carried out either remotely using remote access and remote control software or on-site. A trained operator controls the telescope<sup>54</sup> and the GREGOR adaptive optics system (GAOS).<sup>55,56</sup> HiFI+ is offered as a facility instrument and users are expected to operate the instrument after training. Therefore, an intuitive graphical user

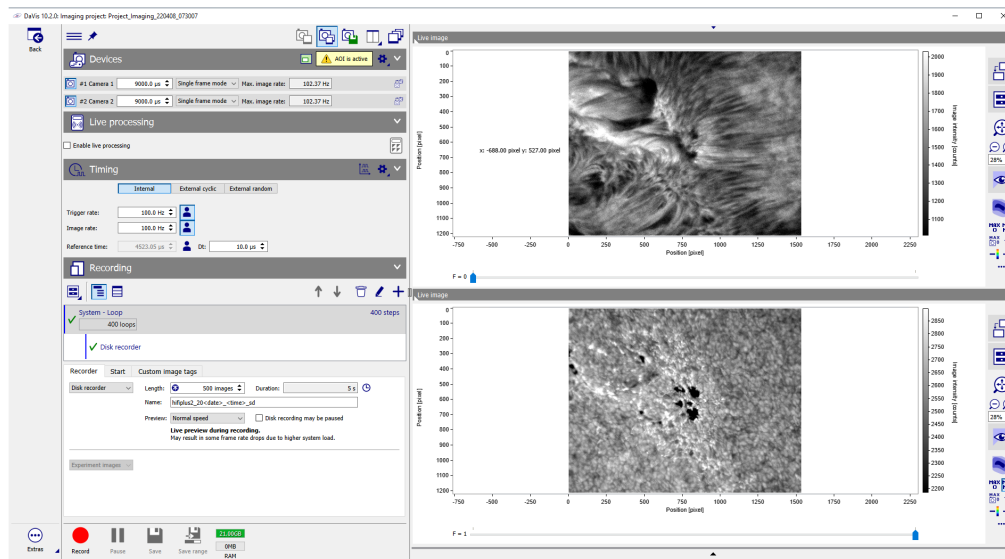


**Fig. 11** User interface of DaVis 10 for multicamera systems. The left side of the application window is reserved for device/camera control and recording parameter, whereas the right side displays live images and offers tools to control the display properties.

interface (GUI) is needed that supports the user to implement and carry out the observing sequences for calibration and science data. In 2022, many experienced observers and novice users worked with the GUI of the DaVis software (Fig. 11) and were able to carry out their observations after one day of training by AIP staff members. A detailed description of HiFI+ and its operations is provided in a comprehensive user manual, and more detailed information is provided in LaVision’s manuals and data sheets for soft- and hardware. The main idea behind the DaVis GUI is to separate device control from displaying images in real-time and image processing. These functions are placed side-by-side in Fig. 11. However, windows, tools, and functions can be arranged in different ways, and they can be shown or hidden so that the user can optimize the GUI layout depending on personal preferences and the type of observations being carried out. The HiFI+ user manual is continuously updated to incorporate best practices and user input.

## 4 Life Cycle of High-resolution Imaging Data

### 4.1 Data Acquisition

The 19.2 TB RAID 0 storage of the HiFI+ Nos. 1 and 3 camera control computers uses eight 2.5-inch Seagate ST2400MM0129 hybrid HDDs with a capacity of 2.4 TB, a spindle speed of 10,000 rpm, and a 12 Gb s<sup>-1</sup> interface for high performance data transfer. The 7.68 TB RAID 0 storage of the HiFI+ No. 2 camera control computer uses eight 2.5-inch Samsung MZ7KH960 SSDs with 960 MB capacity and 6 Gb s<sup>-1</sup> SATA3 interface. These types of RAID 0 storage are capable of writing the imaging data on-the-fly at frame rates of 50 and 100 Hz. Only small delays, mainly for writing header data, are introduced after recording typical science datasets of 500 image pairs, ensuring cadences of 6 and 12 s for loops over such datasets. Thus, depending on camera type, camera settings, and camera control computer, 4 to 10 h of continuous science data can be recorded (see Table 3).

### 4.2 Data Formats

The DaVis software organizes HiFI+ Level 0 data in “imaging projects,” which are sorted by date and time. Each project contains various types of calibration data, i.e., dark, flat-field, defocused flat-field, pinhole, pinhole grid, and target frames. Each calibration set consists of 100 to 2000

individual frames per camera depending on the calibration mode. Only for science data, loops over image sets of 500 frames per camera are invoked. The two Imager sCMOS cameras write sets of 16-bit images, whereas sets of 12-bit images are recorded by the Imager M-lite 2M cameras. In the latter case, pixel packing is used for the 12-bit images, reducing the size of the binary data stream to the RAID 0 storage by 25%. The data are recorded for each camera in native DaVis format, where a small binary header file provides basic image attributes such as image size and digitization depths, and a much larger file contains the binary data of the image set. More detailed information on camera settings and frame attributes can be retrieved from ASCII files written in the extensible markup language (XML). The *sTools* image processing pipeline<sup>57</sup> was significantly updated and now includes routines for reading and decoding DaVis stream data and XML files. The *sTools* software library is publicly available at AIP's GitLab repository ([gitlab.aip.de/cdenker/stools](https://gitlab.aip.de/cdenker/stools)).

Moreover, the pipeline computes average calibration frames, alignment parameters for the imaging channels, and time-series of calibrated and frame-selected science images. The data in native DaVis format are read into the *sTools* image processing pipeline, and the processed data are written in a more commonly used data format. These Level 1 data are saved in the flexible image transport system (FITS)<sup>58,59</sup> format with FITS image extensions.<sup>60</sup> Floating-point data are scaled to 16-bit integer data to preserve disk space, which is appropriate because the input data are also only 12- and 16-bit integer numbers, respectively. The FITS format is commonly used in astronomy and astrophysics, and has been widely adopted in solar physics as well. Metadata consisting of keyword–value pairs, collected in ASCII headers,<sup>61</sup> in combination with extensions for images and tables makes it possible to deliver self-describing data. The structure of the HiFi+ FITS data is illustrated in Fig. 12, which differentiates between calibration and science time-series data. The former typically consists of just a primary header and two extended image extensions for two cameras, whereas the latter includes additionally time-series of alternating image extensions for the two cameras. Common metadata, e.g., information about the telescope and

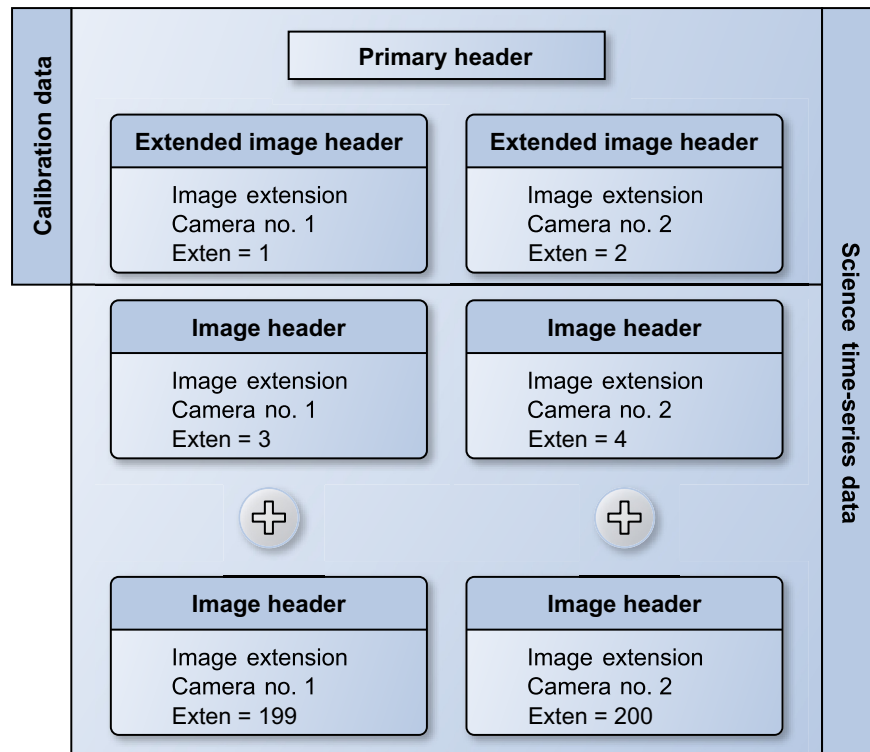


**Fig. 12** Structure of the HiFi+ FITS data products. The level 1.0 data of both cameras are saved in FITS files with image extensions. Calibration data conforms to the FITS structure in the upper box, whereas science time-series data utilizes the compound structure of both boxes, where the circled plus signs indicate the full sequence of typically  $2 \times 100$  image extensions.

**Table 4** Three computing servers are made available by KIS for data processing on-site, i.e., high-resolution imaging data from the three HiFI+ camera systems can be processed in parallel.

	Server No. 1	Server No. 2	Server No. 3
Operating system	CentOS 7.9.2009		
CPU	Intel Xeon E5-4650L	Intel Xeon Silver 4116	
CPU launch date	Second quarter 2012	Third quarter 2017	
Clock speed	2.6 GHz/4 × 8 cores	2.1 GHz/2 × 12 cores	
CPU benchmark	4 × 8415/1457	2 × 14, 785/1678	
Disk storage	196 TB, Dell EMC Isilon		
RAM (GB)	512	128	

observing site, are saved in the primary header. Camera specific information, e.g., detector and filter characteristics, are collected in the first two image extensions, whereas regular image extensions contain mainly information on data statistics and image quality metrics.<sup>47,62</sup>

### 4.3 Data Transfer and Archiving

At the end of the observing day, all data are transferred from the HiFI+ computers to a Dell EMC Isilon storage system with a capacity of about 200 TB, which is provided on site by the Leibniz Institute for Solar Physics (KIS). About 120 TB are available for the temporary storage of HiFI+ data. HiFI+ camera computers and data storage system are linked via an optical 10 Gigabit Ethernet connection. Since RAID 0 was chosen for fast writing, i.e., there is no provision for data loss due to hardware failure, therefore, the data transfer should be immediately started after recording the data. One hour of continuous science data from all three HiFI+ computers amounts to about 7 TB, which takes about 2 h to transfer. Thus, the observed data can be transferred in most cases on the same day. Three data processing servers are made available on site by KIS (see Table 4) to convert the raw Level 0 data to calibrated and frame-selected Level 1 data. In general, only frame-selected data are transferred to the GREGOR archive at AIP.<sup>46</sup> Exceptions are only made for observing sequences of flares and time-series taken under exceptionally good seeing conditions. In these cases, all images are archived in addition to the frame-selected data. Finally, all camera control computers create regular backups of the system partition and user directories that are saved on a dedicated backup server, which is provided by KIS and is available for all instruments at the GREGOR solar telescope and neighboring vacuum tower telescope (VTT). The main computational infrastructure for the GREGOR solar telescope is located at the VTT, where sufficient space is available. The two telescopes are connected via a 10 Gigabit Ethernet connection.

## 5 Science Verification and First-light Observations

Science verification comprised six observing days during the April 4, 2022 to 8 and 11 time period. The first two days were cloudy—actually the observatory was engulfed in clouds while a low pressure system moved through. On April 6, 2022, the first science data were taken with HiFI+. The seeing conditions were good with a Fried-parameter  $r_0 \approx 5 - 10$  cm, and the wind speed was below  $5 \text{ m s}^{-1}$ . The seeing conditions on April 7, 2022, were good and occasionally very good with  $r_0 \approx 5 - 15$  cm and with wind speeds of up to  $15 \text{ m s}^{-1}$ . On April 8, 2022, the seeing deteriorated because of low wind speeds below  $3 \text{ m s}^{-1}$ . The seeing was good with a Fried-parameter  $r_0 \approx 6 - 10$  cm. Wind speeds above  $5 \text{ m s}^{-1}$  prevent warm air to accumulate within the concavity of the retracted dome, which leads to telescope seeing close to the primary mirror. Finally, no observations were taken during the last day of the campaign because of bad seeing conditions.

Various solar activity features are displayed in Figs. 13–18, which were observed on April 7 and 8, 2022, where a total of 378, 1159, and 1084 and 379, 891, and 827 datasets were recorded

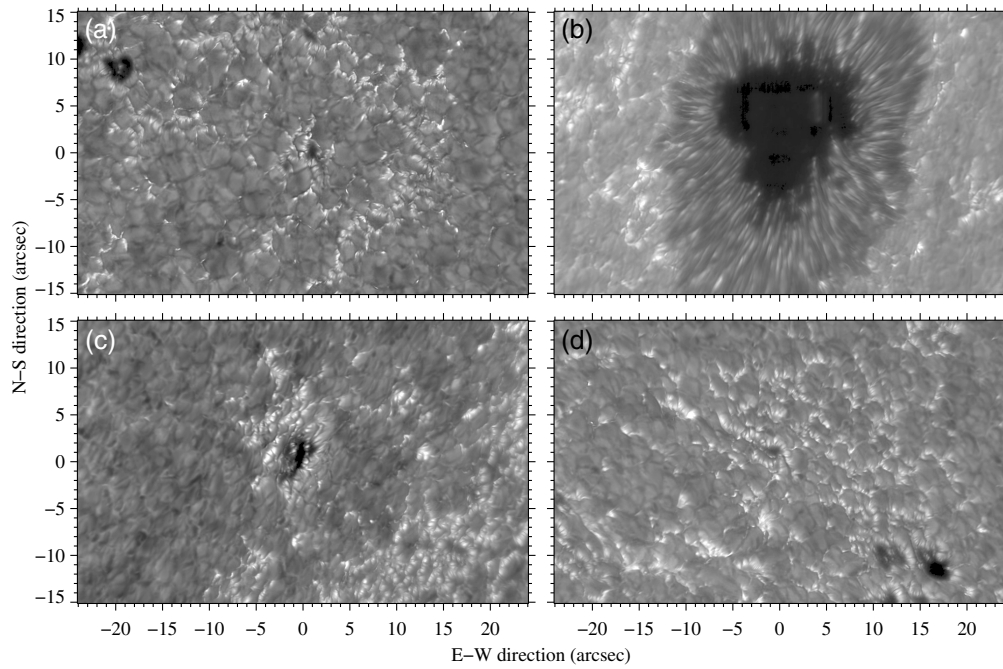


**Fig. 13** Speckle-restored Ca II H images at 396.8 nm of (a) active region NOAA 12985 at 09:07 UT on April 7, 2022, (b) leading spot in active region NOAA 12981 at 09:15 UT on April 7, 2022, (c) trailing pores in active region NOAA 12981 at 11:49 UT on April 7, 2022, and (d) active region NOAA 12983 at 09:19 UT on April 8, 2022.

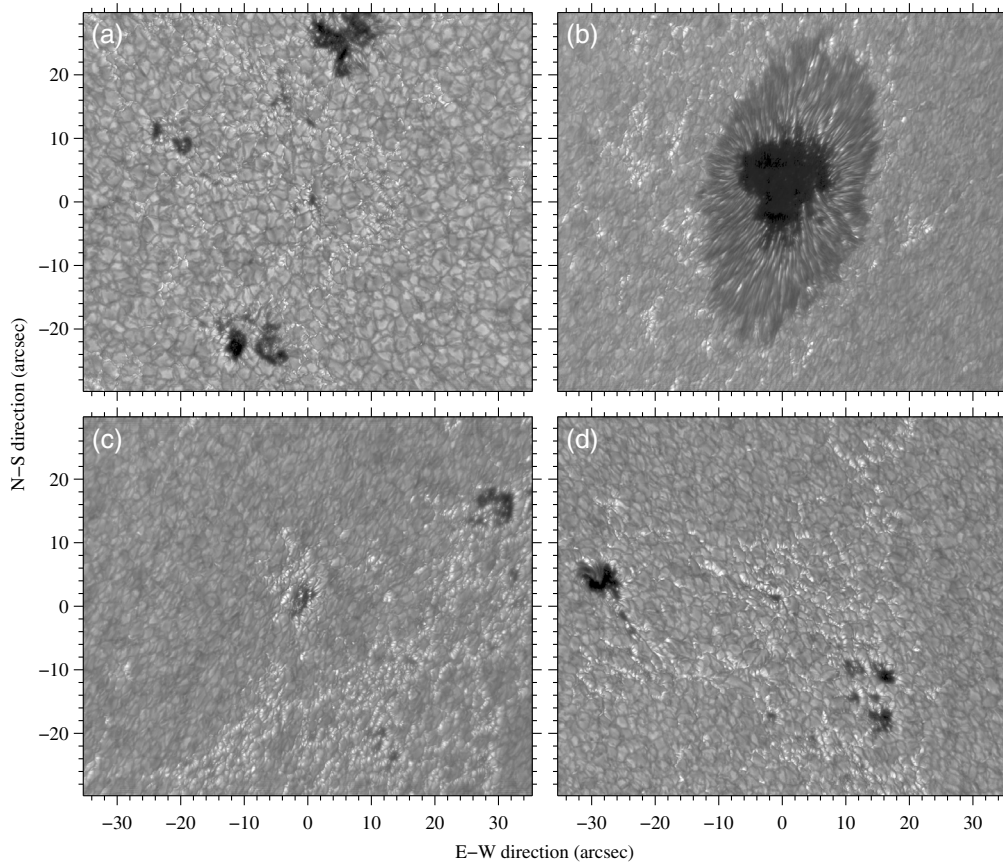


**Fig. 14** (a)–(d) Speckle-restored G-band images at 430.7 nm corresponding to Fig. 13.

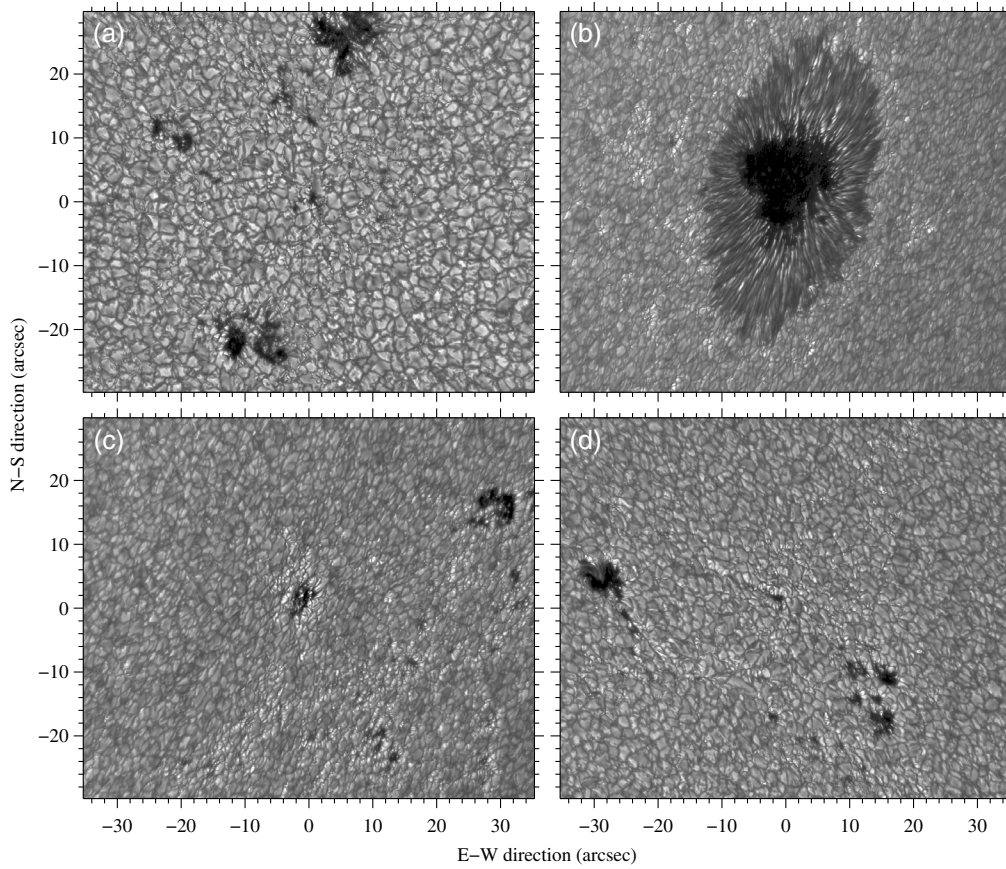


**Fig. 15** (a)–(d) Speckle-restored blue continuum images at 450.6 nm corresponding to Fig. 13.

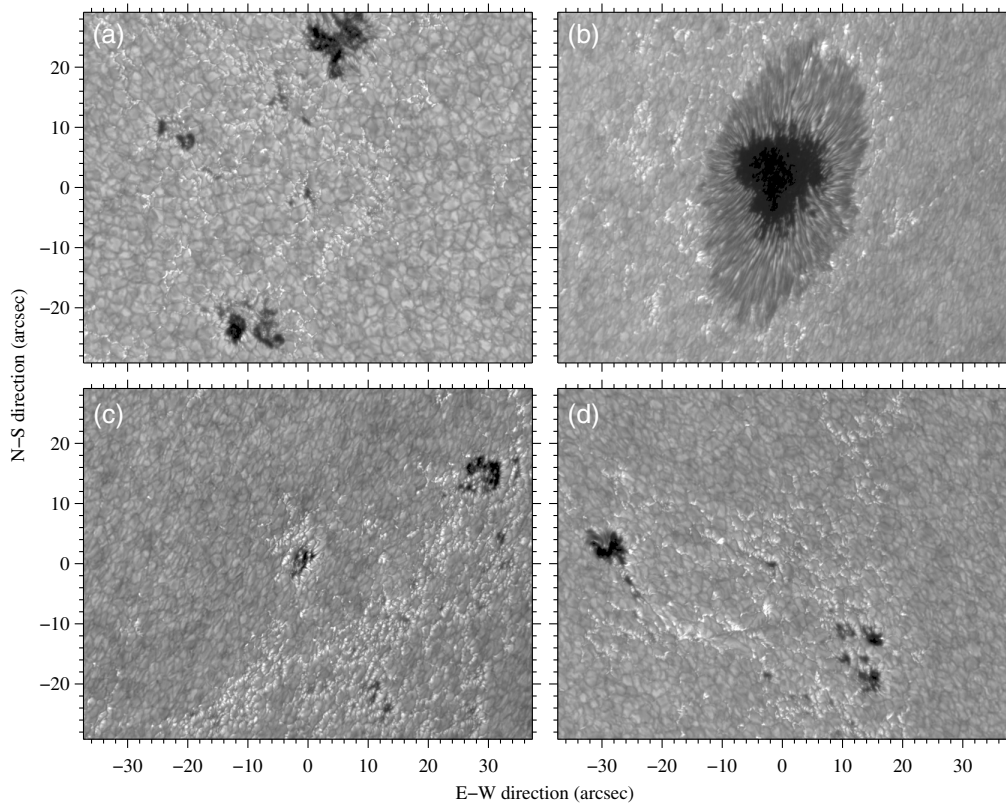


**Fig. 16** (a)–(d) MOMFBD-restored  $H\alpha$  broad-band images at 656.3 nm corresponding to Fig. 13.

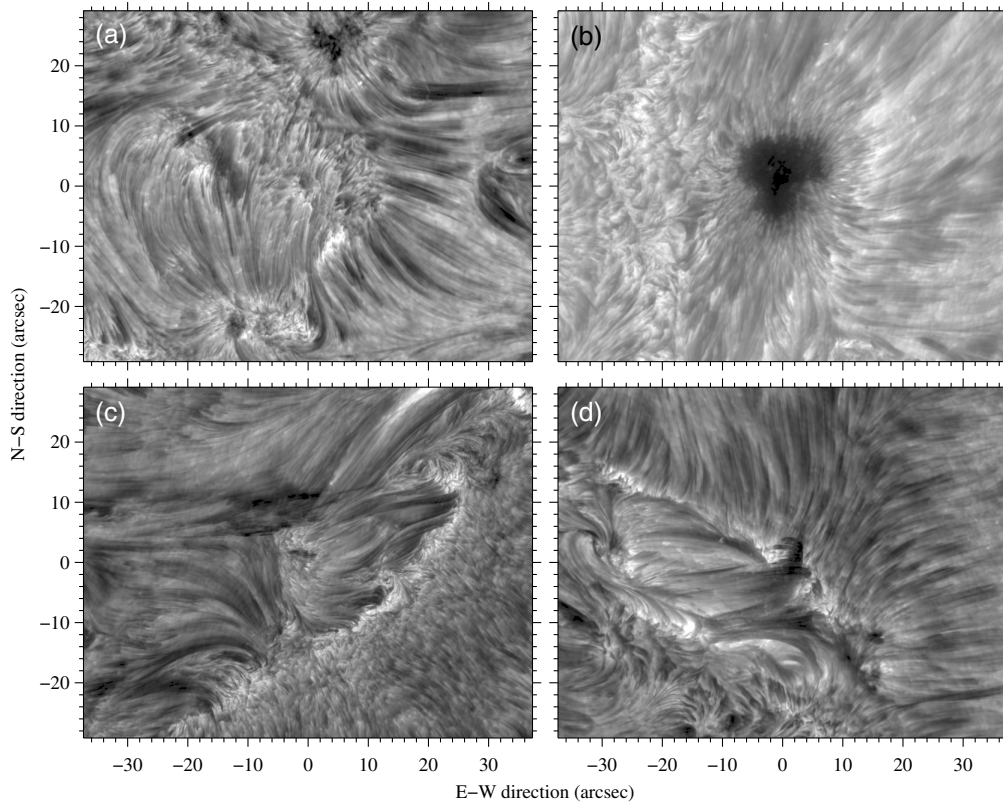


**Fig. 17** (a)–(d) MOMFBD-restored  $H\alpha$  narrow-band images at 656.3 nm corresponding to Fig. 13.

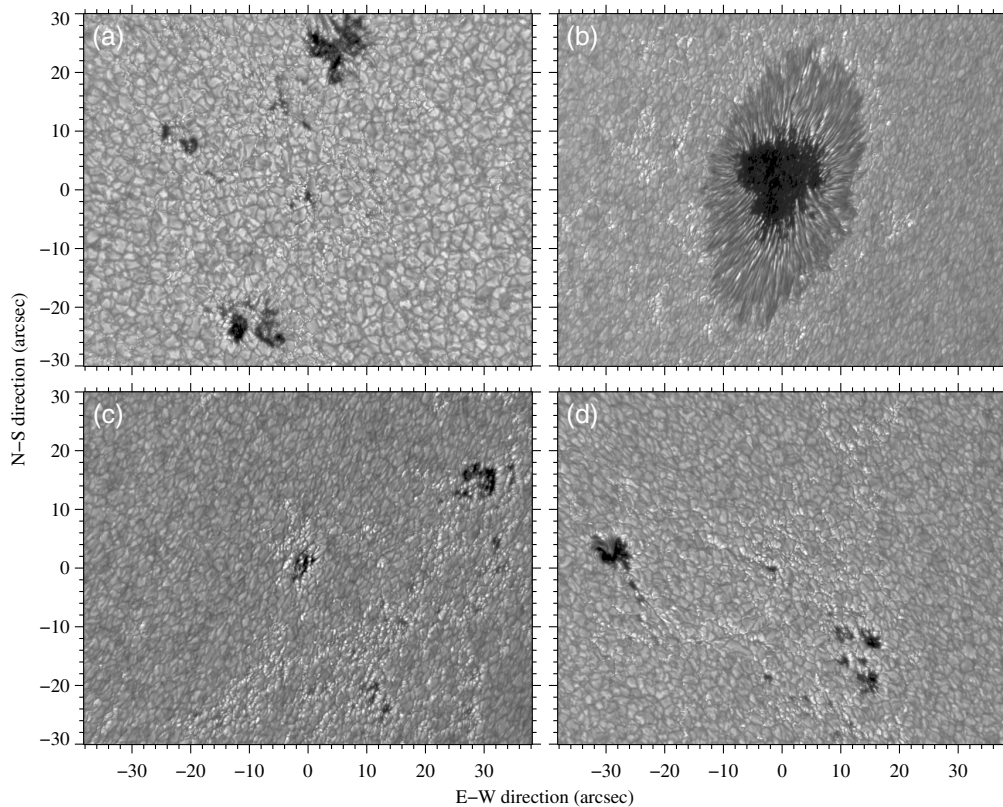


**Fig. 18** (a)–(d) Speckle-restored TiO images at 705.8 nm corresponding to Fig. 13.

with the three HiFI+ camera systems, respectively. Targets with different photospheric and chromospheric morphology were chosen, and a selection of those is depicted for all six wavelength channels, whereby the observing time is the same within a few seconds. The images are displayed using histogram clipping to increase the contrast for better display. Some artifacts are visible in the dark umbra of the sunspot, which was observed close to the solar limb. They arise when the mosaic of isoplanatic patches is assembled after image restoration. If the light level is low, then the alignment of the patches may not be perfect. In addition, the signal-to-noise ratio is small in the darkest part of the umbra so that small intensity differences show up as artifacts in the histogram-clipped images.

To further illustrate the quality of the restored images, Fig. 19 provides a collage of all six imaging channels showing the subarcsecond structure of a micropore.<sup>63</sup> The FOV of  $10'' \times 10''$  exhibits in the neighborhood of the micropore a multitude of small-scale brightenings, which are often aligned in chains within the intergranular lanes. The most notable brightenings occurs at the top-right border of the micropore in the Ca II H image, where filigran fibrils arch away from the micropore. These brightenings are also prominently seen in the broad-band H $\alpha$  image, where mainly the inner line wings of the H $\alpha$  absorption line contribute to the emergent intensity. A small bright kernel is even evident in the H $\alpha$  broadband image, indicating that the bright structure extends to the upper chromosphere. Hints of the brightenings can also be detected in the G-band images, whereas the blue continuum and TiO images only show an inconspicuous small-scale feature at this location. Being able to trace structures through different photospheric and chromospheric layers is a primary goal of HiFI+, as demonstrated in this example of a micropore.

The GREGOR AO system provides the Fried-parameter  $r_0$  as a measure of seeing quality. The  $r_0$  values are derived from the variance of the total mode wavefront error measured by the AO wavefront sensor.<sup>64</sup> The Fried-parameter  $r_0$  and other environmental parameters are available online ([status.tt.iac.es/logs](http://status.tt.iac.es/logs)). Measurements of the Fried-parameter  $r_0$  taken with different instruments and computed with different methods, even when taken at the same site and at the same time, will show significant deviations. Thus, the following discussion is not generally applicable to other solar telescopes. Based on experience at the GREGOR solar telescope, image restoration becomes possible for a Fried-parameter  $r_0 \approx 6$  cm if the AO can lock on a high-contrast feature

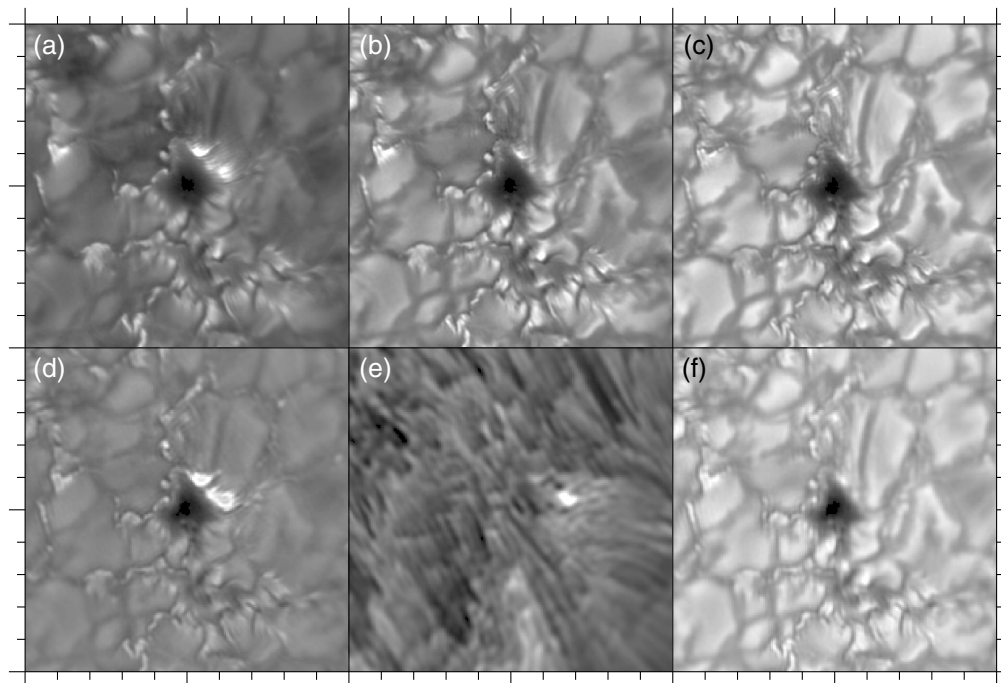


**Fig. 19** Speckle-restored images of a micropore observed in active region NOAA 12985 at 10:51 UT on April 7, 2022, (a) Ca II H image at 396.8 nm, (b) G-band image at 430.7 nm, (c) blue continuum image at 450.6 nm, (d) and (e) H $\alpha$  broad- and narrow-band images at 656.3 nm, and (f) TiO image at 705.8 nm. The FOV is  $10'' \times 10''$ .

such as a pore or the umbra of a small sunspot. Restored images may, however, exhibit restoration artifacts in the periphery of the FOV. Locking on quiet-Sun regions requires a Fried-parameter  $r_0 \approx 8 - 10$  cm. In this case, most of the images in a time-series can be successfully restored. The transition to excellent seeing conditions occurs at a Fried-parameter  $r_0 \approx 12 - 15$  cm. In this case, time-lapse movies of restored images are free of restoration artifacts and are essentially diffraction limited. The best seeing conditions with a Fried-parameter of  $r_0 = 31.7$  cm were encountered on September 10, 2022, which resulted in a much superior image quality compared with the science verification data shown in this article.

## 6 Conclusions

This reference article describes HiFI+ in its configuration in December 2022 at the end of the 2022 observing season. Science verification commenced in April 4 to 11, 2022, as reported in the previous section, which demonstrated that HiFI+ performed according to expectations. The feedback from users in 18 observing campaigns so far was positive. Occasionally reported, synchronization problems of one camera system were solved by a hardware reconfiguration of the PTU. In addition, the RAID 0 HDD storage of two camera control computers was increased by a factor of four. Thus, daily observations are no longer time-limited and cover the time periods with good seeing conditions.

During the 2022A/B observing semesters, i.e., April 6, 2022 to December 2, 2022, HiFI+ data were recorded on 62 days, which resulted in about 90,000 datasets of  $2 \times 100$  frame-selected images, i.e., in total about 18 million science images were stored in the GREGOR archive at AIP and about 90 million science images were recorded with HiFI+. In three cases, all data were kept without frame selection because of excellent seeing conditions on one day and two major flares on the other days. Using the computing resources available at AIP, time-series of images were restored for 14 observing days (HiFI+ Level 2 data). This includes about 52,000 images from all six imaging channels restored with the speckle masking technique and about 20,000  $H\alpha$  narrow- and broad-band images, where image pairs were restored simultaneously using MOMFBD. The grand total of all science and calibration data for the 2022 observing season amounts to about 130 TB.

At the moment, only calibrated HiFI+ Level 1 images are provided in the GREGOR GFPI, HiFI, and HiFI+ data archive at AIP ([gregor.aip.de](http://gregor.aip.de)), which provides a common research environment (CRE)<sup>46</sup> for users of these instruments. These data are embargoed for one year, two years for data related to PhD projects, before they become publicly available. Currently, a bottleneck is the computational effort for image restoration so that only selected datasets can be restored. Restoring a typical HiFI+ dataset for one observing day and for two-synchronized cameras takes 1 to 4 weeks, depending on the duration of the time-series and the chosen image restoration method. Image restoration is typically carried out on desktop computers with AMD Ryzen 9 3950X/5950X CPUs and 64 to 128 GB RAM. In addition, three dedicated computing servers are available with AMD Ryzen 9 3970X(2x)/AMD EPYC 7713 CPUs and 256 GB RAM. An estimate based on the number of restored images so far is that about 40% of the observed data can be restored with the currently available computing resources at AIP. First Level 2 data will become progressively available to the public starting in the second quarter of 2023. Thus, real-time image restoration is an option, which was considered early on for large research infrastructures such as DKIST, where more computing resources are available, delivering data to a Data Center and Archive.<sup>65</sup> However, all things considered, principal investigators of an observing campaign should be able to restore their data themselves using available codes for speckle techniques and blind deconvolution. Fortunately, image restoration based on machine learning techniques is a rapidly evolving field of research, e.g., improving the spatial resolution of solar full-disk images<sup>66</sup> and restoration of high-resolution solar images.<sup>67</sup> Thus, advances in image restoration are expected to lower the computational burden.

In summary, HiFI+ successfully completed commissioning, science verification, and the first observing season as a facility instrument at the GREGOR solar telescope. Data processing of HiFI+ Level 1 data was completed and Level 2 data processing is well underway. First, scientific publications are currently being prepared, and publicly available data will be progressively released starting in the second quarter of 2023.

## Acknowledgments

The 1.5-meter GREGOR solar telescope was built by a German consortium under the leadership of the Leibniz Institute for Solar Physics (KIS) in Freiburg with the Leibniz Institute for Astrophysics Potsdam (AIP), the Institute for Astrophysics Göttingen, and the Max Planck Institute for Solar System Research (MPS) in Göttingen as partners, and with contributions by the Instituto de Astrofísica de Canarias (IAC) and the Astronomical Institute of the Academy of Sciences of the Czech Republic (ASU). The HiFI+ data processing benefits from computational resources, i.e., computing servers, backup server, and Dell Isilon data storage, on-site provided by KIS. We thank AIP's Technical, Project Management, and IT Services sections for their contributions to HiFI+. In addition, we acknowledge the institutional support of all partners and thank all our colleagues who worked hard in recent years to make GREGOR a better telescope. This research has made use of NASA's Astrophysics Data System Bibliographic Services. This study was supported by grants DE 787/5-1, VE 1112/1-1, and KO 6283/2-1 of the Deutsche Forschungsgemeinschaft (DFG), grant 57546881 of the Deutscher Akademischer Austauschdienst (DAAD), and by the European Commission's Horizon 2020 Program under grant agreements 824064 (ESCAPE – European Science Cluster of Astronomy and Particle Physics ESFRI Research Infrastructures) and 824135 (SOLARNET – Integrating High Resolution Solar Physics). CK received funding of the European Union's Horizon 2020 research and innovation program under the Marie Skłodowska-Curie grant agreement No. 895955. We would like to thank the two anonymous reviewers who provided helpful comments and advice improving the manuscript. Thomas Seelemann is employed by LaVision GmbH in Göttingen, where the Imager sCMOS and Imager M-lite 2M cameras, the camera control computers, and the DaVis software were purchased. Beyond this, the authors have no other conflicts of interest to declare that are relevant to the content of this article.

## References

1. P. Qiu et al., "Evaluation of a scientific CMOS camera for astronomical observations," *Res. Astron. Astrophys.* **13**, 615–628 (2013).
2. A. G. Basden, "Analysis of electron multiplying charge coupled device and scientific CMOS readout noise models for Shack–Hartmann wavefront sensor accuracy," *J. Astron. Telesc. Instrum. Syst.* **1**, 039002 (2015).
3. I. A. Steele et al., "Experiments with synchronized sCMOS cameras," *Proc. SPIE* **9915**, 991522 (2016).
4. T. R. Rimmele and J. Marino, "Solar adaptive optics," *Living Rev. Sol. Phys.* **8**, 2 (2011).
5. C. Denker, A. Tritschler, and M. Löfdahl, "Image restoration," in *Encyclopedia of Optical and Photonic Engineering*, C. Hoffman and R. Driggers, Eds., 2nd ed., pp. 1–9, CRC Press (2015).
6. K. G. Puschmann and M. Sailer, "Speckle reconstruction of photometric data observed with adaptive optics," *Astron. Astrophys.* **454**, 1011–1019 (2006).
7. C. Denker et al., "Field-dependent adaptive optics correction derived with the spectral ratio technique," *Sol. Phys.* **241**, 411–426 (2007).
8. M. Steinegger et al., "The new global high-resolution H $\alpha$  network. First observations and first results," in *Proc. 1st Solar and Space Weather Euroconf.: The Solar Cycle and Terrest. Clim., Solar and Space Weather*, A. Wilson, Ed., ESA Special Publication, Vol. 463, pp. 617–622 (2000).
9. W. Cao et al., "Diffraction-limited polarimetry from the infrared imaging magnetograph at Big Bear Solar Observatory," *Publ. Astron. Soc. Pac.* **118**, 838–844 (2006).
10. T. J. Kentischer et al., "ChroTel: a robotic telescope to observe the chromosphere of the Sun," *Proc. SPIE* **7014**, 701413 (2008).
11. B. Lyot, "Le Filtre Monochromatique Polarisant et ses Applications en Physique Solaire," *Ann. d'Astrophys.* **7**, 31–79 (1944).
12. Y. Öhman, "A new monochromator," *Nature* **141**, 157–158 (1938).
13. J. M. Beckers, L. Dickson, and D. Woodman, "Cinematography of solar intensity, velocity, and magnetic fields," *Opt. Eng.* **14**, 140164 (1975).

14. W. Cao et al., “Scientific instrumentation for the 1.6 m New Solar Telescope in Big Bear,” *Astron. Nachr.* **331**, 636–639 (2010).
15. F. Wöger, “DKIST visible broadband imager interference filters,” *Proc. SPIE* **9147**, 91479I (2014).
16. C. R. de Boer, “Speckle-Interferometrie und ihre Anwendung auf die Sonnenbeobachtung,” PhD thesis, Georg-August Universität Göttingen, Germany (1993).
17. O. von der Lühe, “Speckle imaging of solar small scale structure. I. Methods,” *Astron. Astrophys.* **268**, 374–390 (1993).
18. F. Wöger and O. von der Lühe, “KISIP: a software package for speckle interferometry of adaptive optics corrected solar data,” *Proc. SPIE* **7019**, 70191E (2008).
19. C. U. Keller and O. von der Lühe, “Solar speckle polarimetry,” *Astron. Astrophys.* **261**, 321–328 (1992).
20. M. G. Löfdahl, “Multi-frame blind deconvolution with linear equality constraints,” *Proc. SPIE* **4792**, 146–155 (2002).
21. M. van Noort, L. Rouppe van der Voort, and M. G. Löfdahl, “Solar image restoration by use of multi-frame blind deconvolution with multiple objects and phase diversity,” *Sol. Phys.* **228**, 191–215 (2005).
22. D. B. Jess et al., “ROSA: a high-cadence, synchronized multi-camera solar imaging system,” *Sol. Phys.* **261**, 363–373 (2010).
23. F. Wöger et al., “The Daniel K. Inouye Solar Telescope (DKIST)/visible broadband imager (VBI),” *Sol. Phys.* **296**, 145 (2021).
24. T. R. Rimmele et al., “The Daniel K. Inouye Solar Telescope – observatory overview,” *Sol. Phys.* **295**, 172 (2020).
25. C. Denker, “Instrument and data analysis challenges for imaging spectropolarimetry,” *Astron. Nachr.* **331**, 648–651 (2010).
26. W. Schmidt et al., “The 1.5 meter solar telescope GREGOR,” *Astron. Nachr.* **333**, 796–809 (2012).
27. C. Denker et al., “A retrospective of the GREGOR solar telescope in scientific literature,” *Astron. Nachr.* **333**, 810–815 (2012).
28. F. Kneer, “Hopes and expectations with GREGOR,” *Astron. Nachr.* **333**, 790–795 (2012).
29. M. Collados et al., “GRIS: the GREGOR infrared spectrograph,” *Astron. Nachr.* **333**, 872–879 (2012).
30. K. G. Puschmann et al., “The GREGOR Fabry–Pérot interferometer,” *Astron. Nachr.* **333**, 880–893 (2012).
31. O. von der Lühe et al., “The GREGOR broad-band imager,” *Astron. Nachr.* **333**, 894–900 (2012).
32. L. Kleint et al., “GREGOR: optics redesign and updates from 2018–2020,” *Astron. Astrophys.* **641**, A27 (2020).
33. H. Künzel, “Polarisationsinterferenzfilter und ihre Prüfung,” *Astron. Nachr.* **282**, 252–256 (1955).
34. C. Denker et al., “Solar physics at the Einstein Tower,” *Astron. Nachr.* **337**, 1105–1113 (2016).
35. M. Estribeau and P. Magnan, “Fast MTF measurement of CMOS imagers using ISO 12333 slanted-edge methodology,” *Proc. SPIE* **5251**, 243–252 (2004).
36. C. B. Markwardt, “Non-linear least-squares fitting in IDL with MPFIT,” in *Astronomical Data Analysis Software and Systems XVIII*, D. A. Bohlender, D. Durand, and P. Dowler, Eds., ASP Conference Series, Vol. **411**, pp. 251–254 (2009).
37. H. Neckel and D. Labs, “The solar radiation between 3300 and 12500 Å,” *Sol. Phys.* **90**, 205–258 (1984).
38. H. Neckel, “Announcement – spectral atlas of solar absolute disk-averaged and disk-center intensity from 3290 to 12510 Å now available from Hamburg observatory anonymous FTP site,” *Sol. Phys.* **184**, 421 (1999).
39. L. Wallace et al., “Infrared spectral atlases of the Sun from NOAO,” *Astrophys. J. Suppl. Ser.* **106**, 165–169 (1996).
40. T. E. Berger and A. M. Title, “On the relation of G-band bright points to the photospheric magnetic field,” *Astrophys. J.* **553**, 449–469 (2001).

41. S. Jafarzadeh et al., “Migration of Ca II H bright points in the internetwork,” *Astron. Astrophys.* **563**, A101 (2014).
42. Y. Liu et al., “Studies of isolated and non-isolated photospheric bright points in an active region observed by the new vacuum solar telescope,” *Astrophys. J.* **856**, 17 (2018).
43. C. Denker et al., “The GREGOR Fabry-Pérot interferometer: a new instrument for high-resolution solar observations,” *Proc. SPIE* **7735**, 77356M (2010).
44. M. Verma and C. Denker, “Measuring the etalon quality of the GREGOR Fabry-Pérot interferometer,” *J. Astron. Telesc. Instrum. Syst.* **6**, 015001 (2020).
45. K. G. Puschmann et al., “GREGOR Fabry-Pérot interferometer and its companion the blue imaging solar spectrometer,” *Opt. Eng.* **52**, 081606 (2013).
46. C. Denker et al., “Data analysis and management for high-resolution solar Physics – image restoration and imaging spectroscopy at the GREGOR solar telescope,” *Astrophys. J. Suppl. Ser.* **236**, 5 (2018).
47. C. Denker et al., “Image quality in high-resolution and high-cadence solar images,” *Sol. Phys.* **5**, 236 (2018).
48. LaVision, *Data Sheet Imager sCMOS*, LaVision GmbH, Göttingen (2020).
49. LaVision, *Data Sheet Imager M-lite 2M*, LaVision GmbH, Göttingen (2021).
50. LaVision, *Product Manual for Imager M-lite*, LaVision GmbH, Göttingen (2020).
51. LaVision, *Product Manual for Imager sCMOS*, LaVision GmbH, Göttingen (2020).
52. LaVision, *Product Manual for Programmable Timing Unit (PTU X)*, LaVision GmbH, Göttingen (2021).
53. LaVision, *Product Manual for DaVis 10.2 Software*, LaVision GmbH, Göttingen (2021).
54. C. Halbgewachs et al., “The GREGOR telescope control system,” *Astron. Nachr.* **333**, 840–846 (2012).
55. T. Berkefeld et al., “Adaptive optics development at the German solar telescopes,” *Appl. Opt.* **49**, G155–G166 (2010).
56. T. Berkefeld et al., “The GREGOR adaptive optics system,” *Astron. Nachr.* **333**, 863 (2012).
57. C. Kuckein et al., “sTools – a data reduction pipeline for the GREGOR Fabry-Pérot interferometer and the high-resolution fast imager at the GREGOR solar telescope,” in *Fine Structure and Dynamics of the Solar Atmosphere*, S. Vargas Domnguez et al., Eds., Vol. 327, pp. 20–24 (2017).
58. D. C. Wells, E. W. Greisen, and R. H. Harten, “FITS – a flexible image transport system,” *Astron. Astrophys. Suppl. Ser.* **44**, 363–370 (1981).
59. R. J. Hanisch et al., “Definition of the flexible image transport system (FITS),” *Astron. Astrophys.* **376**, 359–380 (2001).
60. J. D. Ponz, R. W. Thompson, and J. R. Munoz, “The FITS image extension,” *Astron. Astrophys. Suppl. Ser.* **105**, 53–55 (1994).
61. S. V. H. Haugan and T. Fredvik, “SOLARNET metadata recommendations for solar observations,” arXiv:2011.12139 (2020).
62. H. Deng et al., “Objective image-quality assessment for high-resolution photospheric images by median filter-gradient similarity,” *Sol. Phys.* **290**, 1479–1489 (2015).
63. S. J. González Manrique, N. Bello González, and C. Denker, “High-resolution imaging spectroscopy of two micro-pores and an arch filament system in a small emerging-flux region,” *Astron. Astrophys.* **600**, A38 (2017).
64. D. Sprung et al., “Characterization of optical turbulence at the GREGOR solar telescope: temporal and local behavior and its influence on the solar observations,” *Proc. SPIE* **10002**, 1000205 (2016).
65. A. Beard, F. Wöger, and A. Ferayorni, “Real-time speckle image processing with the DKIST,” *Proc. SPIE* **11452**, 114521X (2020).
66. C. J. Daz Baso and A. Asensio Ramos, “Enhancing SDO/HMI images using deep learning,” *Astron. Astrophys.* **614**, A5 (2018).
67. P. Jia et al., “Solar image restoration with the CycleGAN based on multi-fractal properties of texture features,” *Astrophys. J. Lett.* **881**, L30 (2019).

**Carsten Denker** is head of the “Solar Physics” section and the solar observatory “Einstein Tower” at the Leibniz Institute for Astrophysics Potsdam (AIP) and adjunct professor at the

University Potsdam. He holds a doctoral degree in physics and a diploma in social sciences from the University of Göttingen. He is the instrument PI of GFPI, HiFI+, and FaMuLUS. His research efforts concentrate on solar magnetic fields and activity, sunspots, space weather, imaging spectropolarimetry, and image restoration.

**Meetu Verma** is a post-doctoral researcher in the “Solar Physics” at the Leibniz Institute for Astrophysics Potsdam (AIP). She received her doctoral degree in physics from the University Potsdam in 2013. Thereafter, she worked for one year as a post-doctoral researcher at Max Planck Institute for Solar System Research in Göttingen. Her research interests cover high-resolution studies of solar magnetic features using multi-instruments and multi-wavelength observations. She has extensive experience in organizing coordinated observing campaigns.

**Aneta Wiśniewska** is a post-doctoral researcher in the “Solar Physics” at the Leibniz Institute for Astrophysics Potsdam (AIP). She holds a doctoral degree in natural sciences from the University of Freiburg, which she gained while working at the Leibniz Institute for Solar Physics (KIS). Her research focuses on helioseismology, global magnetic activity of the Sun, solar flares, space weather, image correction, signal analysis, and spectroscopic observations.

**Robert Kamlah** is a doctoral student in the “Solar Physics” section at the Leibniz Institute for Astrophysics Potsdam (AIP). He started his doctoral studies in spring 2020, and his research focuses on photospheric and chromospheric magnetic and flow fields. The emphasis of his research project is on analyzing three-dimensional flow fields of emerging and decaying active regions.

**Ioannis Kontogiannis** is a post-doctoral researcher in the “Solar Physics” section of the Leibniz Institute for Astrophysics Potsdam (AIP). He holds a doctoral degree in natural sciences from the National and Kapodistrian University of Athens, Greece. He is leading two research projects, funded by DAAD/IKYDA and DFG. His research focuses on the dynamics of the quiet Sun (small-scale magnetism, chromospheric structures, and waves), the prediction of solar flares and the evolution of solar active regions.

**Ekaterina Dineva** is a junior post-doctoral researcher in the “Solar Physics” section at the Leibniz Institute for Astrophysics Potsdam (AIP). She holds a doctoral degree in astrophysics from the University Potsdam and a diploma in business management from the University of National and World Economy, Bulgaria. Her research topics are long- and short-term solar activity, solar cycles, Sun-as-a-star spectroscopy, and solar-stellar connections. Furthermore, she has experience in the field of solar radio physics and space weather.

**Jürgen Rendtel** is a technical staff member in the “Solar Physics” section at the Leibniz Institute for Astrophysics Potsdam (AIP). He received his doctoral degree in physics from the University Potsdam. He is involved in research and development of instruments for high-resolution solar physics at AIP and responsible for the optical laboratory at the solar “Einstein Tower.” He is a founding member of the International Meteor Organization (IMO), where he served as the President for 25 years.

**Svend-Marian Bauer** is a mechanical engineer in the Technical Section at the Leibniz Institute for Astrophysics Potsdam (AIP) and has a Dipl.-Ing (FH) degree in the field of precision engineering. He participated in national and international projects focusing on astronomical post-focus instrumentation: multi-object spectrograph MUSE for the European Southern Observatory (ESO), high-resolution spectrograph PEPSI at the Large Binocular Telescope (LBT) at Mt. Graham in Arizona, and STELLA robotic telescopes for stellar activity and GREGOR Solar Telescope in Tenerife.

**Mario Dionies** is a member of the technical staff at the “IT Services” of the at the Leibniz Institute for Astrophysics Potsdam (AIP). His expertise is in information security and the installation and configuration of Windows systems including network components, backup management, and data protection.

**Hakan Önel** is head of the “Technical Section” at the Leibniz Institute for Astrophysics Potsdam (AIP). He holds a doctoral degree in astrophysics from the Potsdam University and has been involved in the designing, manufacturing, maintenance, verification, and commissioning activities of predominantly ground-based focal instruments as well as instruments for space missions as Solar Orbiter.

**Manfred Woche** obtained his diploma in physics at the Friedrich Schiller University Jena in 1976. Until 1996, he was employed at the Karl Schwarzschild Observatory Tautenburg. From 1996 until 2001, he worked in optical design and astronomical instrumentation for different institutes, especially for the Max Planck Institute for Extraterrestrial Physics Garching and the Skinakas Observatory Crete. Since 2001, he has been responsible for the optical design of astronomical instrumentation at the Leibniz Institute for Astrophysics Potsdam (AIP).

**Christoph Kuckein** is a post-doctoral researcher funded by a Marie Skłodowska-Curie fellowship since September 2021 at the “Solar Physics” group of the Instituto de Astrofísica de Canarias (IAC). He holds a doctoral degree in astrophysics from the University of La Laguna (Spain) and worked for about 9 years at the Leibniz Institute for Astrophysics Potsdam (AIP). His research is mainly focused on the interpretation of chromospheric phenomena using inversion tools and spectropolarimetric data.

**Thomas Seelemann** studied physics at the Georg August University Göttingen. For his diploma thesis and doctoral dissertation, he worked at the Max Planck Institute for Fluid Dynamics in Göttingen in the field of molecular physics and received his doctoral degree in 1980. Since then, he has been employed at LaVision GmbH in Göttingen, where he works on cameras and their integration into dedicated experimental applications.

**Partha S. Pal** is an associate professor in the Department of Physics, Bhaskaracharya College of Applied Sciences, University of Delhi, India, where he teaches physics and mathematics. He received his doctoral degree in physics from the University of Delhi in 2010. His current research interests cover digital image analysis, statistical analysis, and machine learning in astronomy and astrophysics. He was visiting scientist in the “Solar Physics” at the Leibniz Institute for Astrophysics Potsdam (AIP) from 2018 to 2022.